CENTRO DE INVESTIGACIONES
EN OPTICA, A.C.

"GAUSSIAN PROBE BEAM WITH HIGH SPHERICAL ABERRATION FOR REFRACTIVE INDEX MEASUREMENTS IN LIQUID SAMPLES. AN APPLICATION TO GLUCOSE CONCENTRATION"

Thesis submitted in fulfillment of the requirements for the
Ph.D. degree in science (Optics)

Presents: **M. Sc. Etna Dafne Yánez Roldán**

Advisor: Dr. Moisés Cywiak Garbarcewicz

Final version

León · Guanajuato · México
Septiembre de 2020

Acknowledgments

I want to acknowledge the help and guidance of my advisor, Professor Dr. Cywiak, whose enthusiasm, exceptional patience, and invaluable support have made my work achievable.

My thanks also to Dr. Flores, Dr. Moreno, and Dr. Malacara Doblado, for their well-aimed suggestions and reviews during evaluations

Thanks to my reviewers and friends for their support.

Thanks also to all CIO staff who have kindly provided all of the requested resources to complete this project.

Thanks to CONACYT for financial support.

Finally, I thank my loved family and God.

Abstract

In this thesis, we introduce a novel, accurate optical technique for measuring refractive indexes of liquid transparent or turbid samples using the diffractive properties of spherical aberrated Gaussian beams. The heights of the primary side-lobes of the normalized intensity profiles measured at a plane of observation in a near vicinity around the focal region of a lens permit attaining with high accuracy and repeatability the index of refraction of the samples under inspection. We demonstrate analytically and experimentally that, as the technique relies on the diffracted properties of the Gaussian beam transmitted through the samples under test, the measurements are immune to noise and external environmental conditions. The sensitivity of the technique can easily be modified making it useful to different applications. We exemplify the use of the technique by applying it to glucose concentration measurements due to its importance in the medical, biological, and industrial fields. Further examples can be found in applications in which the determination of the concentration can be used to describe the purity of solutions in the pharmaceutical and medical areas, as well as pollution, communication materials, and substances for the food industry.

The technique can be tuned at different concentrations ranges according to a required specific application by simply modifying the initial set up. Our experimental results are analytically compared with theoretical models to allow measuring analytically the performance of the optical system. For this purpose, we use the Fresnel Gaussian shape invariant method (FGSI), which founds to be appropriate for calculating with high accuracy the overall diffraction propagation process, starting from the illuminating source beam, through the optical components of the optical system and up to a plane of observation.

In the case of high sensitivity measurements, our experimental results were compared with reference data in a Clarke error grid. The changes in glucose concentrations fall appropriately in the range of clinical tests demonstrating the relevance of our optical technique for medical applications.

List of Figures

2.1. Propagation with the Fresnel diffraction integral……………………………………………..9

2.2. Gaussian intensity distributions at three distances of propagation………………………………………………………………………………………..12

2.3. Bsinc intensity distributions in the plane of observation………………………..…16

2.4. Stable and unstable resonators…………………………………………………………..17

2.5. Confocal resonator…………………………………………………………………………..22

2.6. Transverse modes TEM_{mn} ……………………………………………………………26

2.7. Zero-order Gaussian beam in a confocal resonator…………………………………...28

2.8. Homodyne detector…………………………………………………………………………33

3.1. Optical setup for changes of concentration at large concentrations………………...36

3.2. Analytical normalized intensity distributions calculated by FGSI for the first setup……………………………………………………………………………………………38

3.3. Analytical normalized intensity distributions obtained by FGSI with misalignment……………………………………………………………………………………..40

3.4. Experimental normalized intensity distributions for the first setup…………………..43

3.5. Heights as a function of glucose concentration for the first setup…………………44

3.6. Experimental normalized intensity distributions in turbid media……………..…46

3.7. Optical setup that uses an SLSC for improving sensitivity……………………………47

3.8. Analytical normalized intensity profiles calculated by FGSI for the second setup…..49

3.9. Analytical normalized intensity profiles calculated by FGSI for a beam free of aberrations………………………………………………………………………………………50

3.10. Experimental normalized intensity distributions for the second setup………………..51

3.11. Analytical normalized intensity distribution calculated by FGSI with a polynomial term……………………………………………………………………………………………53

3.12. Experimental heights as a function of glucose concentration for the second setup……………………………………………………………………………………………..55

3.13. Clarke Error Grid……………………………………………………………………..…57

Table of contents

Acknowledgments ii

Abstract iii

List of Figures iv

1. Introduction 1

2. Theoretical Framework 4

- 2.1Wave equation solution 4
- 2.2 Fresnel Diffraction Integral 8
- 2.3 Examples of propagation using the Fresnel diffraction integral. 10
  - 2.3.1 Example 1. Propagation of a Gaussian distribution 10
  - 2.3.2 Example 2. Propagation of a Circ distribution 10
- 2.4 Optical Resonator 17
  - 2.4.1 Hermite polynomes 18
  - 2.4.2 Modes in a confocal resonator 21
- 2.5 Fresnel Gaussian shape invariant (FGSI) 29
- 2.6 Homodyne detector 32

3. An application for glucose concentration measurements 35

- 3.1 Theoretical glucose measurements 35
- 3.2 Experimental glucose measurements 41
- 3.3 Theoretical glucose measurements replacing the lens by a singlet-lens-shaped container (SLSC) 47
- 3.4 Experimental glucose measurements performed with a singlet-lens-shaped container (SLSC) 51

4. Conclusions 58

Bibliography 59

1. Introduction

The refractive index is an important optical property of materials that are used to characterize them. For example, some applications can be found in which determination of the concentration can be used to describe the purity of solutions in the pharmaceutical and medical areas, as well as pollution, communication materials, and substances for the food industry [1, 2, 3]. In this thesis, we introduce a novel and accurate optical technique for measuring the refractive index of transparent liquid samples. The technique can be tuned at different concentrations ranges according to a required specific application by simply modifying the initial set up. For example, if the measurements should require measurements in accuracy steps of 100 mg/dl, as shown in the next section, the sample under test will be placed in a cuvette containing it, and a focusing lens will be used to produce the aberrated focused beam. In contrast, if a very high accuracy step is required for example of the order of l0 mg/dl, then, the liquid sample is introduced in a focusing lens-shaped container to produce the aberrated focused Gaussian beam.

The optical technique presented here is based on the diffractive properties of the propagated aberrated beam which are immune to external noise or even to changes on ambient conditions [4], allowing to obtain the measurements with high repeatability. Then, the optical system described in this thesis provides reliable results even for the case of high sensitivity requirements. We exemplify the feasibility and repeatability of the technique in the field of glucose concentration measurements by measuring different glucose concentrations of transparent and turbid samples in liquid tri-distilled water solutions. We use controlled laboratory conditions for our illustrative experiments to attain feasible comparisons between our technique and other optical techniques. Different techniques in this field have been proposed as photoacoustic [5, 6], NIR and MIR spectroscopy [7, 8], Raman spectroscopy [9], kromoscopy [10], polarimetric [11], OCT [12], fluorescence [13], NIR optoacoustic spectroscopy [14] and multispectral photoacoustic sensing [15].

In general, most of these optical techniques are based in the acquisition of a single, low signal to noise ratio signal, requiring additional complex numerical processing to extract substantial data to attain the measurements [16, 17]. As a consequence, when the measurements have to be performed in an industrial ambient or under high sensitivity requirements, the reliability of the measurements decreases.

The optical technique introduced here overcomes the above limitation, as it is based on the inherent diffractive properties of a propagated Gaussian beam. As it is well-known, the diffractive characteristics of a beam, that can be calculated, with good accuracy by means of the Fresnel diffraction integral, depend only on the path of propagation and on the beam wavelength. The intensity profile that is calculated after the propagation of a Gaussian beam is well characterized and stable, and it remains unaffected, even under changes of the refractive index of the air where the beam propagates. Thus, measurements that depend only on the diffractive properties of a propagated beam, in principle, are expected to be highly stable, potentially providing high repeatability. Furthermore, a technique that takes advantage of these characteristics will not depend on a single signal. On the contrary, as the intensity profile of a propagated beam has a unique shape, the measurements so obtained result highly reliable. Moreover, if the measurements are based on the normalized intensity profiles, the power of the illuminating beams does not affect the measurements.

The optical technique described in the following sections consists of measuring the vertical heights of the primary side-lobes of the normalized intensity profiles of the propagated Gaussian probe beam in which high spherical aberration has been introduced intentionally. Furthermore, it is only necessary to determine the relative height of only one of the lateral side-lobes. The measurements are taking at a plane of observation once that the beam has been transmitted through the liquid sample under test. We remark, that the measurements can also be obtained even for turbid samples. Furthermore, the side-lobes of the aberrated beam exhibit such a high sensitivity, that glucose concentrations in steps as small as 10 mg/dl can be obtained. Measurements with such a high sensitivity may result in a challenge for reliable measurements by other optical techniques.

To obtain the spherically aberrated Gaussian probe beam, a large area of the front surface of a convex-plane singlet lens is illuminated. The diffractive normalized intensity profiles so obtained are acquired utilizing a dedicated homodyne profiler, specially designed in our lab for this purpose. This detector allows enhancing, even more, the accuracy and reliability of the measurements.

We also show in the following sections, that the width variations of the probe beam attributable to the laser cavity do not affect the measurements. Should Gaussian beam widths occur, these are negligible for the Gaussian He-Ne laser, as demonstrated in the next section, thus, maintaining unaffected the results.

Our experimental results are analytically compared with theoretical models to allow measuring analytically the performance of the optical system. For this purpose, we use the Fresnel Gaussian shape invariant method (FGSI) [18-21], which founds to be appropriate for calculating with high accuracy the overall diffraction propagation process, starting from the illuminating source beam, through the optical components of the optical system and up to a plane of observation. In the next chapter, we provide our theoretical description.

2. Theoretical Framework

As our optical system fits well with the scalar paraxial diffractive model, for sustaining properly our theoretical analysis, it will be convenient to first demonstrate that the Fresnel diffraction integral is an exact solution of the paraxial wave Helmholtz differential equation.

2.1 Wave equation

The scalar Helmholtz differential equation can be written as,

$$\nabla^2\Psi(x,y,z) + {k_0}^2\Psi(x,y,z) = 0. \tag{2.1}$$

In Equation (2.1), $k_0 = \frac{2\pi}{\lambda}$, represents the wave number and λ represents the wavelength of the illuminating source. The function $\Psi(x,y,z)$ represents the amplitude distribution of the field in a three-dimensional coordinate space.

As the field propagates mainly in the z direction, which corresponds to the optical axis, it is possible to propose a solution for $\Psi(x,y,z)$ in a separable expression as,

$$\Psi(x,y,z) = f(x,y,z)\exp(ik_0 z). \tag{2.2}$$

We now proceed in calculating the first and second derivatives of Equation (2.2) with respect to z as follows,

$$\frac{\partial\Psi}{\partial z} = ik_0 f(x,y,z)\exp(ik_0 z) + \frac{\partial f(x,y,z)}{\partial z}\exp(ik_0 z), \tag{2.3}$$

$$\frac{\partial^2\Psi}{\partial z^2} = -k_0 f(x,y,z) exp(ik_0 z) + 2ik_0\frac{\partial f(x,y,z)}{\partial z} exp(ik_0 z) + \frac{\partial^2 f(x,y,z)}{\partial z^2}\exp(ik_0 z)\,. \tag{2. 4}$$

Substituting the derivatives given by Equations (2.3) and (2.4) into Equation (2.1), we obtain,

$$\frac{\partial^2 f}{\partial x^2} + \frac{\partial^2 f}{\partial y^2} + \left[-k_0^2 f + 2ik_0 \frac{\partial f}{\partial z} + \frac{\partial^2 f}{\partial z^2}\right] + k_0^2 f = 0\,. \tag{2.5}$$

As the curvature of the field can be neglected because the propagation has already been considered in the expression of Equation (2.1), we can assume for practical purposes that $\frac{\partial^2 f}{\partial z^2} \ll \frac{\partial f}{\partial z}$. This approximation is known as a paraxial approximation. Then, upon neglecting the term $\frac{\partial^2 f}{\partial z^2}$ in Equation (2.5), one obtains,

$$\nabla^2 f(x, y, z) + 2ik_0 \frac{\partial f(x,y,z)}{\partial z} = 0. \tag{2.6}$$

Equation (2.6) can be rewritten as,

$$-\left(\frac{\partial^2 f}{\partial x^2} + \frac{\partial^2 f}{\partial y^2}\right) = 2ik_0 \frac{\partial f}{\partial z}\,. \tag{2.7}$$

It may result interesting to notice that the Equation (2.7) has the following Schrödinger wave equation shape,

$$-\frac{\hbar^2}{2m} \nabla^2 \Psi = i\hbar \frac{\partial \Psi}{\partial t}\,. \tag{2.8}$$

To solve the paraxial approximation of the Helmholtz differential Equation (2.8), or equivalently its Schrödinger equivalent equation, we will consider the Fourier transform of $f(x, y, z)$ and its corresponding inverse Fourier transform $F(u, v, z)$,

$$f(x, y, z) = \iint_{-\infty}^{\infty} F(u, v, z) \exp[i2\pi(ux + vy)]\, du\, dv\ , \tag{2.9}$$

and,

$$F(u, v, z) = \iint_{-\infty}^{\infty} f(x, y, z) \exp[-i2\pi(ux + vy)]\, dx\, dy. \tag{2.10}$$

The corresponding derivatives for $f(x, y, z)$ in Equation (2.9) are,

$$\frac{\partial^2 f}{\partial x^2} = \iint_{-\infty}^{\infty} (-4\pi^2 u^2) F(u, v, z) \exp[i2\pi(ux + vy)]\, du\, dv, \tag{2.11}$$

$$\frac{\partial^2 f}{\partial y^2} = \iint_{-\infty}^{\infty} (-4\pi^2 v^2) F(u, v, z) \exp[i2\pi(ux + vy)]\, du\, dv, \tag{2.12}$$

and,

$$\frac{\partial f}{\partial z} = \iint_{-\infty}^{\infty} \frac{\partial F(u,v,z)}{\partial z} \exp[i2\pi(ux+vy)]\, du\, dv\,. \tag{2.13}$$

In Equations (2.9 - 2.13), u and v correspond to the spatial frequency of x and y respectively.

Substituting Equations (2.11-2.13) in the paraxial approximation, Equation (2.7) reads,

$$\iint_{-\infty}^{\infty} \left\{-4\pi^2(u^2+v^2)F(u,v,z) + 2ik_0\frac{\partial F(u,v,z)}{\partial z}\right\} \exp[i2\pi(ux+vy)]\, du\, dv = 0\,. \tag{2.14}$$

From Equation (2.14), one obtains,

$$\left\{-4\pi^2(u^2+v^2)F(u,v,z) + 2ik_0\frac{\partial F(u,v,z)}{\partial z}\right\} = 0\,. \tag{2.15}$$

Equation (2.15) can be solved as follows. First, Equation (2.15) is written as,

$$\frac{4\pi^2}{2ik_0}(u^2+v^2)F(u,v,z) = \frac{\partial F(u,v,z)}{\partial z}. \tag{2.16}$$

Then, using $k_0 = \frac{2\pi}{\lambda}$ allows rewriting Equation (2.16) as

$$-i\pi\lambda(u^2+v^2)\partial z = \frac{\partial F(u,v,z)}{F(u,v,z)}. \tag{2.17}$$

Equation (2.17) can then be solved, we obtain,

$$-(u^2+v^2)i\pi\lambda z + C = \ln F. \tag{2.18}$$

From Equation (2.18) we now obtain,

$$exp[-c - i\pi\lambda z(u^2+v^2)] = F(u,v,z) = Aexp[-i\pi\lambda z(u^2+v^2)]. \tag{2.19}$$

And finally, Equation (2.19) gives,

$$F(u,v,z) = G(u,v)exp[-i\pi\lambda z(u^2+v^2)]. \tag{2.20}$$

If in Equation (2.20), $z=0$ then $F(u,v,0) = G(u,v)$, so Equation (2.19) can be rewritten as

$$F(u,v,z) = F(u,v,0)exp[-i\pi\lambda z(u^2+v^2)]. \tag{2.21}$$

Substituting $F(u,v,z)$ given in Equation (2.21) in Equation (2.9) gives,

$$f(x,y,z) = \iint_{-\infty}^{\infty} F(u,v,0)exp[-i\pi\lambda z(u^2+v^2)]\exp\,[i2\pi(ux+vy)]\,du\,dv. \tag{2.22}$$

Now, calculating the Fourier transform of Equation (2.22) gives,

$$f(x,y,z) = \mathcal{F}\{F(u,v,0)exp[-i\pi\lambda z(u^2+v^2)]\}. \tag{2.23}$$

In solving Equation (2.23), we find that,

$$f(x,y,z) = \mathcal{F}^{-1}\{F(u,v,0)\}\otimes\mathcal{F}^{-1}\{exp[-i\pi\lambda z(u^2+v^2)]\}. \tag{2.24}$$

In Equation (2.24) the symbol ⊗ represents the operation of convolution. Equation (2.24) can readily be rewritten as,

$$f(x,y,z) = f(x,y,0)\otimes\mathcal{F}^{-1}\{exp[-i\pi\lambda z(u^2+v^2)]\}. \tag{2.25}$$

Equation (2.25) can also be written as,

$$f(x,y,z) = f(x,y,0)\otimes\frac{1}{i\lambda z}exp\left[-\frac{\pi}{i\lambda z}(x^2+y^2)\right]. \tag{2.26}$$

Now, Equation (2.26) is rewritten as,

$$f(x,y,z) = f(x,y,0)\otimes\frac{1}{i\lambda z}exp\left[\frac{i\pi}{\lambda z}(x^2+y^2)\right]. \tag{2.27}$$

And Equation (2.27) gives,

$$f(x,y,z) = \frac{1}{i\lambda z}\iint_{-\infty}^{\infty} f(\xi,\eta,0)exp\left\{\frac{i\pi}{\lambda z}[(x-\xi)^2+(y-\eta)^2]\right\}d\xi d\eta. \tag{2.28}$$

Using Equation (2.28) allows writing $\Psi(x,y,z)$ as,

$$\Psi(x,y,z)=\frac{exp(ikz)}{i\lambda z}\iint_{-\infty}^{\infty}f(\xi,\eta,0)exp\left(\frac{i\pi}{\lambda z}[(x-\xi)^2+(y-\eta)^2]\right)d\xi d\eta. \quad (2.29)$$

Equation (2.29) is relevant and physically it is referred to as the Fresnel Diffraction Integral [22, 23], and it is an analytical exact solution of the paraxial Helmholtz differential equation [24].

The solution given by the Equation (2.29) is expressed in terms of $f(\xi,\eta,0)$. As no restrictions were made on this function in the above calculations, it can, therefore, be any arbitrary well-behaved function at the initial plane, without any restrictions. The Equation (2.29) may be regarded as a generator of solutions of the paraxial wave equation.

We can now proceed to calculate accurately the propagation of beams using the Fresnel diffraction integral, as described in the next section.

2.2 Fresnel Diffraction Integral

One of the most useful tools to calculate the propagation of beams in the scalar, the paraxial model is represented by the Fresnel diffraction integral [22, 23]. Although, as demonstrated in section 2.1, this integral represents a generator of solutions of the Schrödinger type differential equation. The Fresnel diffraction integral can be used to describe accurately the propagation of beams, thus, obtaining the diffraction patterns of experimental observations.

To perform the propagation analytically with the Fresnel diffraction integral, the initial field $\Psi_I(x,y)$ is located at an initial plane with coordinates $(x,y,z=0)$. Then, at a distance z a plane of observation is placed and has coordinates $(\xi,\eta,z=z)$. Both planes are parallel between them as depicted in Fig.(2.1). The amplitude distribution of the propagated field $\Psi_F(\xi,\eta)$ is obtained as

$$\Psi_F(\xi,\eta) = \frac{exp(ikz)}{\sqrt{i\lambda z}} \iint_{-\infty}^{\infty} \Psi_I(x,y)\, exp\left(\frac{i\pi}{\lambda z}[(x-\xi)^2 + (y-\eta)^2]\right) dx\, dy \tag{2.30}$$

where $i = \sqrt{-1}$, and λ is the wavelength of the illuminating field.

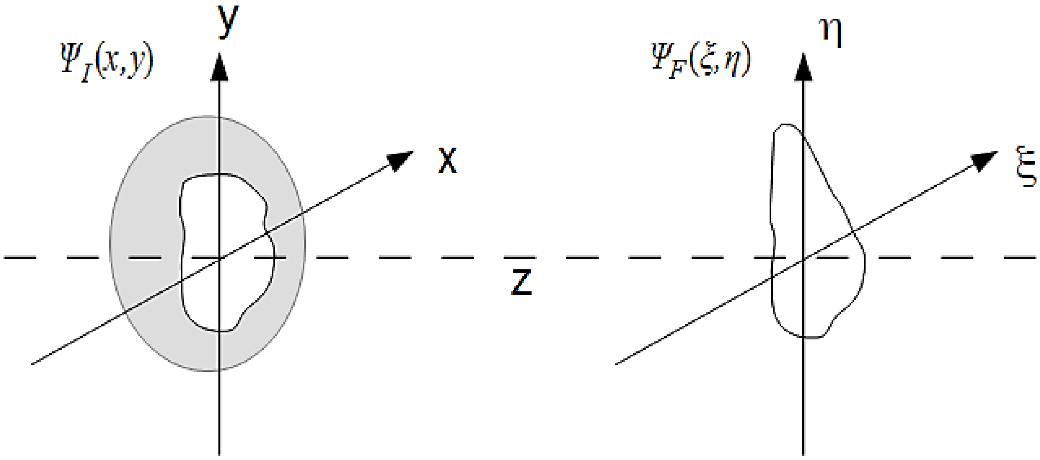

Fig. 2.1. Propagation with the Fresnel diffraction integral. Initial field $\Psi_I(x,y)$ at a plane $(x,y,z=0)$ and its corresponding distribution $\Psi_F(\xi,\eta)$ in a plane of observation $(\xi,\eta,z=z)$ once it has been propagated a z distance.

By expanding the quadratic terms, allows rewriting Equation (2.30) as,

$$\Psi_F(\xi,\eta) = \frac{exp(ikz)}{\sqrt{i\lambda z}} exp\left(\frac{i\pi}{\lambda z}(\xi^2+\eta^2)\right) \times \iint_{-\infty}^{\infty} \Psi_I(x,y)\, exp\left(\frac{i\pi}{\lambda z}(x^2+y^2)\right) exp\left(-\frac{i2\pi}{\lambda z}(x\xi + y\eta)\right) dx\, dy\,. \tag{2.31}$$

In Equation (2.31), using the Fourier transform notation gives,

$$\Psi_F(\xi,\eta) = \frac{exp(ikz)}{\sqrt{i\lambda z}} exp\left(\frac{i\pi}{\lambda z}(\xi^2+\eta^2)\right) \mathcal{F}\left\{\Psi_I(x,y) \exp\left(\frac{i\pi}{\lambda z}(x^2+y^2)\right)\right\}. \tag{2.32}$$

The Fresnel diffraction integral given by Equation (2.32) is used to calculate the propagation of beams. In our experiments, the illuminating source is a laser beam with a Gaussian intensity profile. At the plane of observation, our specially dedicated homodyne detector obtains the propagated intensity profile. For descriptive purposes, in the next section, we provide the corresponding analytical bases to propagate some type of beams. This study will help us to support our theoretical model.

2.3 Propagation examples of some beams by using the Fresnel diffraction integral.

For brevity of our description, the majority of our examples will be one-dimensional.

2.3.1 Example 1: Propagation of a Gaussian beam

The amplitude of a Gaussian distribution at the initial plane can be written as

$$\Psi(x) = exp\left(-\left(\frac{x}{r_0}\right)^2\right), \tag{2.33}$$

where r_0 is its semi-width.

Substituting the amplitude given by Equation (2.33) in the Fresnel diffraction integral, Equation (2.30) gives,

$$\Psi(\xi) = \frac{exp(ikz)}{\sqrt{i\lambda z}} \int_{-\infty}^{\infty} exp\left(-\left(\frac{x}{r_0}\right)^2\right) exp\left(\frac{i\pi}{\lambda z}(x-\xi)^2\right) dx\,. \tag{2.34}$$

Expanding the quadratic phase in the Equation (2.34) gives,

$$\Psi(\xi) = \frac{exp(ikz)}{\sqrt{i\lambda z}} exp\left(\frac{i\pi}{\lambda z}\xi^2\right) \int_{-\infty}^{\infty} exp\left(-\pi x^2\left(\frac{\lambda z - i\pi}{\pi {r_0}^2} - \frac{i}{\lambda z}\right)\right) exp\left(\frac{i2\pi}{\lambda z}x\xi\right) dx. \tag{2.35}$$

Now, introducing the parameter $u = \frac{\pi}{\lambda z}$ in Equation (2.35) gives,

$$\Psi(\xi) = \frac{exp(ikz)}{\sqrt{i\lambda z}} exp\left(\frac{i\pi}{\lambda z}\xi^2\right) \mathcal{F}\left\{exp\left(-\pi x^2\left(\frac{\lambda z - i\pi {r_0}^2}{\pi {r_0}^2 \lambda z}\right)\right)\right\}\Bigg|_{u=\frac{\xi}{\lambda z}}. \qquad (2.36)$$

Finally, we rewrite Equation (2.36) as,

$$\Psi(\xi) = \frac{exp(ikz)}{\sqrt{i\lambda z}} \cdot \sqrt{\frac{\pi {r_0}^2 \lambda z}{\lambda z - i\pi {r_0}^2}} \cdot exp\left(\frac{i\pi}{\lambda z}\xi^2\right) exp\left(-\pi\left(\frac{\pi {r_0}^2 \lambda z}{\lambda z - i\pi {r_0}^2}\right)\left(\frac{\xi}{\lambda z}\right)^2\right). \qquad (2.37)$$

Equation (2.37) is the expression of the amplitude distribution at the plane of observation. To better visualize the implications given by Equation (2.37), we rewrite it as

$$\Psi(\xi) = \frac{exp(ikz)}{\sqrt{i\lambda z}} \cdot \sqrt{\frac{\pi {r_0}^2 \lambda z}{\lambda z - i\pi {r_0}^2}} exp\left(\frac{i\pi}{\lambda z}\xi^2\right) exp\left(-\pi^2 {r_0}^2\left(\frac{\lambda z + i\pi {r_0}^2}{\lambda^2 z^2 + \pi^2 {r_0}^4}\right)\frac{\xi^2}{\lambda z}\right). \qquad (2.38)$$

Now, it is possible to define the complex constant term,

$$A = \frac{exp(ikz)}{\sqrt{i\lambda z}} \sqrt{\frac{\pi {r_0}^2 \lambda z}{\lambda z - i\pi {r_0}^2}}\ , \qquad (2.39)$$

And the semi-width r of the Gaussian beam as,

$$r = r_0\sqrt{1 + \frac{\lambda^2 z^2}{\pi^2 {r_0}^4}}\ . \qquad (2.40)$$

Additionally, it is possible to define the radius of curvature R as,

$$R = \frac{\lambda^2 z^2 + \pi^2 {r_0}^4}{\lambda^2 z}\ . \qquad (2.41)$$

Equations (2.39 – 2.41) allows rewriting Equation (2.38) as,

$$\Psi(\xi) = Aexp\left(-\frac{\xi^2}{r^2}\right) exp\left(i\frac{\pi}{\lambda}\frac{\xi^2}{R}\right). \qquad (2.39)$$

It will be noticed from the Equation (2.39), that $\Psi(\xi)$, at the observation plane, is also a Gaussian distribution with amplitude A and with a quadratic phase. The Gaussian behavior at the plane of observation is given by the real exponential expression. If the distance of propagation z increases, the semi-width r of the Gaussian beam increases accordingly, while its amplitude A is adjusted according to the energy of the beam that must be preserved. Fig. (2.2) depicts how the Gaussian beam intensity distribution evolves as it propagates along the z distance. The amplitude distribution at the plane of observation has unique characteristics as a function of the semi width due only to the diffractive properties as obtained analytically utilizing the Fresnel diffraction integral. It has to be remarked that the experimental results compare well with this integral, demonstrating its usefulness to calculate experimental observations, even though it is a paraxial approximation solution.

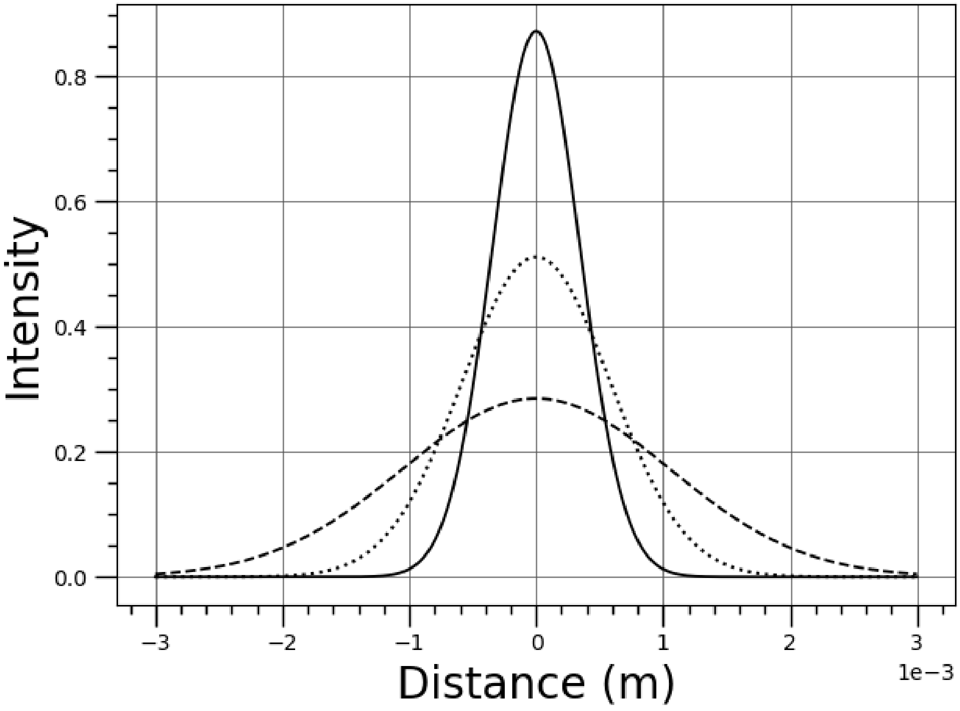

Fig. 2.2. Gaussian intensity distributions at three distances of propagation. The continuous line plot is at $z = 1$ m, the dotted line plot is at $z = 3$ m and the dashed line plot is at $z = 6$ m, $r_0 = 6 \times 10^{-4}$ m and $\lambda = 638 \times 10^{-9}$ m.

2.3.2 Example 2: Propagation of a Circ function.

The Circ function is widely used in optics. It is useful to characterize optical apertures of lenses, especially for the case of spherical lenses or circular mirrors with finite size. The Circ function is usually used for truncating and diffracting light. In this section, we will consider the diffraction due to these circular components utilizing the Fresnel diffraction integral.

The Circ function is defined as,

$$\mathrm{Circ(r)} = \begin{cases} 1 & \text{if } \mathrm{r} < a \\ 0 & \text{otherwise} \end{cases} . \tag{2.40}$$

In Equation (2.40),

$$\mathrm{r} = \sqrt{x^2 + y^2}, \tag{2.41}$$

and a represents the radius of the circular aperture.

The amplitude distribution $\Psi(\xi, \eta)$ at the observation plane with coordinates $(\xi - \eta)$ can be calculated using the Fresnel diffraction integral,

$$\Psi(\xi, \eta) = \frac{exp(ikz)}{\sqrt{i\lambda z}} \iint_{-\infty}^{\infty} \Psi(x, y)\, exp\left(\frac{i\pi}{\lambda z}[(x - \xi)^2 + (y - \eta)^2]\right) dx\, dy\, . \tag{2.42}$$

It is convenient to introduce the following change of variables for solving the above integral Equation (2.42),

$$x = \rho \cos \emptyset\, ,\ y = \rho \sin \emptyset, \tag{2.43}$$

$$\xi = r \cos \Theta\, ,\ \eta = r \sin \Theta. \tag{2.44}$$

With the variables defined by Equations (2.43) and (2.44) $\Psi(x, y)$ in Equation (2.42) will become now a function of (ρ, ϕ). We will also assume radial symmetry. Thus, the amplitude distribution becomes a one-variable function as, $\Psi(\rho)$.

Under the above conditions, Equation (2.42) can now be written as

$$\Psi(\xi,\eta) = \frac{exp(ikz)}{\sqrt{i\lambda z}} exp\left(\frac{i\pi}{\lambda z} r^2\right) \times \int_0^\infty \Psi(\rho)\rho\, d\rho\, exp\left(\frac{i\pi}{\lambda z} r^2\right) \int_0^{2\pi} \mathrm{d}\emptyset\, exp\left(-\frac{i2\pi}{\lambda z} r\rho\, cos(\emptyset - \Theta)\right). \tag{2.45}$$

Using the integral definition of the Bessel function of the first kind, zero-order J_0,

$$J_0(a) = \frac{1}{2\pi}\int_0^{2\pi} exp(-ia\, cos(\emptyset - \Theta))\, d\emptyset. \tag{2.46}$$

Using equation (2.46) allows rewriting Equation (2.45) as,

$$\Psi(\xi,\eta) = \frac{exp(ikz)}{i\lambda z} exp\left(\frac{i\pi}{\lambda z} r^2\right) 2\pi \int_0^\infty \Psi(\rho) exp\left(\frac{i\pi}{\lambda z}\rho^2\right) J_0\left(\frac{2\pi}{\lambda z} r\rho\right) \rho\, d\rho\,. \tag{2.47}$$

Equation (2.47) cannot be solved analytically, thus, it has to be estimated by numerical algorithms. At long distances of propagation, it is possible to neglect the quadratic phase in the integral of Equation (2.47). When this is the case, this approximation is referred to as the Fraunhofer diffraction. Then, neglecting the term $exp\left(\frac{i\pi}{\lambda z}\rho^2\right)$ allows writing the integral in Equation (2.47) as

$$\Psi(\xi,\eta) = \frac{exp(ikz)}{i\lambda z} exp\left(\frac{i\pi}{\lambda z} r^2\right) 2\pi \int_{\rho=0}^{\rho=a} \Psi(\rho)\, J_0\left(\frac{2\pi}{\lambda z} r\rho\right) \rho\, d\rho\,. \tag{2.48}$$

Now, to solve the integral given by Equation (2.48), we make the following change of variables

$$s = \frac{2\pi}{\lambda z} r\rho, \tag{2.49}$$

$$\frac{\lambda}{2\pi r} ds = d\rho \,. \tag{2.50}$$

Using Equations (2.49) and (2.50) allows rewriting Equation (2.48) as,

$$\Psi(r) = \left(\frac{\lambda z}{2\pi r}\right)^2 \int_{s=o}^{s=\frac{2\pi}{\lambda z} ra} sJ_0(s)\, ds. \tag{2.51}$$

To calculate the integral in Equation (2.51), we will use the following property,

$$\int_0^b x\, J_0(\mathrm{x}) dx = xJ_1(x)|_0^b \,, \tag{2.52}$$

Using Equation (2.52) allows writing Equation (2.51) as,

$$\Psi(r) = a^2 \frac{J_1\left(\frac{2\pi}{\lambda z} ra\right)}{\left(\frac{2\pi}{\lambda z} ra\right)} \,. \tag{2.53}$$

Using the definition of the Bessel-sinc, Bsinc(x) function, $\mathrm{Bsinc}(x) = \frac{J_1(x)}{x}$, allow us to write finally Equation (2.53) as

$$\Psi(r) = a^2 \mathrm{Bsinc}\left(\frac{2\pi}{\lambda z} ra\right) . \tag{2.54}$$

The following Fig.(2.3) depicts how the Bsinc function given by Equation (2.54) evolves at different z distances.

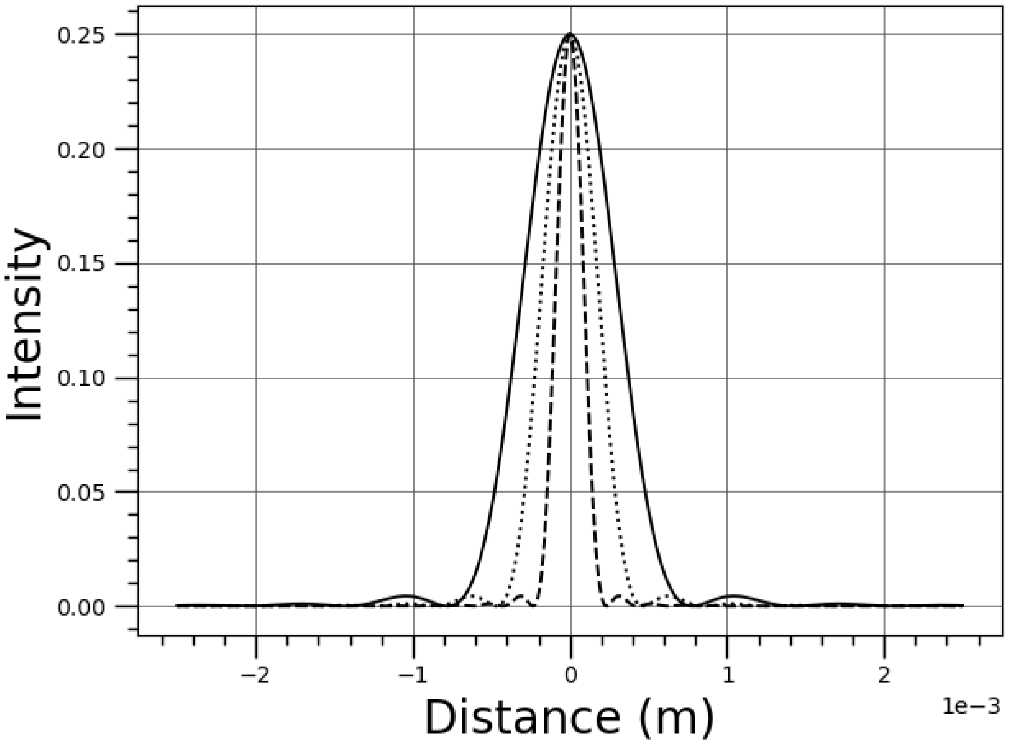

Fig. 2.3. Bsinc intensity distributions at the plane of observation. The continuous line plot is for $z = 1$ m, the dotted line plot is for $z = 3$ m and the dashed line plot is for $z = 6$ m; $a = 5 \times 10^{-3}$ m and $\lambda = 638 \times 10^{-9}$ m.

By comparing experimental results with the theoretical calculations obtained, it results apparently that the Fresnel diffraction integral describes appropriately the amplitude distribution of the diffracted fields for different z distances of propagation. If the index of refraction should change across the optical arrangement the Fresnel diffraction integral can also be used to calculate the propagation at the plane of observation. In our particular case, the change of the index of refraction occurs in the sample under test due to different concentrations. Thus, the amplitude distribution at the plane of detection will be sensitive and related to its diffractive properties allowing it to detect changes in the refractive indexes.

In the next section, we will emphasize the stability of our optical detection system, showing that changes in the semi-width due to the laser cavity will be practically undetectable. The radiation traveling inside the optical cavity is described with the Hermite-Gaussian solutions for the paraxial wave equation, resulting in Gaussian modes beams at the output. In our experiments, we have used only the zero-order Gaussian beam of a commercially available He-Ne laser.

2.4 Optical resonator

An optical resonator essentially consists of two end mirrors separated by a distance L allowing a beam of light to propagate through the resonator cavity as depicted in Fig. (2.4). Assuming that the gain medium does not affect the electromagnetic modes of the laser resonator, it is possible to consider that there is only free space between them [25]. The light inside the cavity propagates, diffracts, bounces off the mirrors many times and passes through optical components, so if there are misalignments problems, or the curvature of the mirrors or the distance separating them are such that there might be some leaks from the resonator after many reflections, the optical resonator will be unstable. In contrast, stable resonators are those where these parameters are such that the light propagates in a parallel path to the optical axis during successive round trips without escaping.

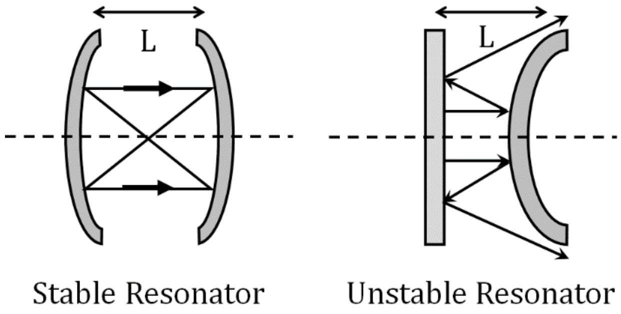

Fig. 2.4. Stable and unstable resonators

An understanding of laser modes propagating inside resonators can be obtained by the paraxial wave equation. In particular, we will show that Hermite-Gaussian beams are solutions of these cases and are referred to as modes of free-space propagation. Before proceeding further, we find it convenient to introduce some mathematical properties of the Hermite polynomials.

2.4.1 Hermite polynomials

Hermite functions are of interest because they are solutions to eigenvalue problems like those that arise in the quantum harmonic oscillator [26].

The Hermite polynomials $H_n(x)$ satisfy the differential equation

$$y(x)'' - 2xy(x)' + 2ny(x) = 0. \tag{2.55}$$

We will show, that the differential Equation (2.55) has solutions $y(x)$ that can be obtained by means the generating function,

$$g(x,t) = exp(2xt - t^2) = \sum_{n=0}^{\infty} H_n(x) \left(\frac{t^n}{n!}\right). \tag{2.56}$$

In Equation (2.56) $H_n(x)$ are the well-known Hermite polynomials. From Equation (2.55) we find that the recurrence relations are,

$$H_{n+1}(x) = 2xH_n(x) - 2\mathrm{n}H_{n-1}(x), \tag{2.57}$$

and,

$$H_n'(x) = 2nH_{n-1}(x). \tag{2.58}$$

From the Rodrigues representation

$$H_n(x) = (-1)^n exp(-x^2)\frac{d^n}{dx^n} exp(-x^2), \tag{2.59}$$

we obtain $H_0(x) = 1$ and $H_1(x) = 2x$. The recursive Equations (2.57 - 2.58) allows the construction of any desired polynomial, $H_n(x)$.

Now, we will calculate the Fourier transform of the Hermite polynomials. We start by considering the following Fourier transform expression,

$$F\left\{H_n(x)exp\left(-\frac{x^2}{2}\right)\right\}, \tag{2.60}$$

The transform in Equation (2.60) in integral form is written as,

$$\int_{-\infty}^{\infty} H_n(x)exp\left(-\frac{x^2}{2}\right)exp(-ix\xi)dx. \tag{2.61}$$

To solve Equation (2.61), we substitute the Hermite polynomials $H_n(x)$ given by Equation (2.56) in Equation (2.61) to obtain

$$\begin{aligned}\sum_{n=0}^{\infty}\left(\frac{t^n}{n!}\right)\int_{-\infty}^{\infty} H_n(x)exp\left(-\frac{x^2}{2}\right)exp(-ix\xi)dx \\ = \int_{-\infty}^{\infty} \exp(2xt - t^2)exp\left(-\frac{x^2}{2}\right)exp(-ix\xi)dx\,.\end{aligned} \tag{2.62}$$

We now complete the perfect square in Equation (2.62), and now we define the following integral,

$$I = exp(-t^2)\int_{-\infty}^{\infty} exp\left(-\frac{1}{2}(x-2t)^2 - 4t^2\right)exp(-ix\xi)dx. \tag{2.63}$$

To solve the integral in Equation (2.63) we will use the following Fourier properties

$$F\{f(x)\} = F(u)\,, \tag{2.64}$$

$$F\{f(x-x_0)\} = exp(-i2\pi x_0)F(u)\,, \tag{2.65}$$

$$F\{exp(-\pi x^2)\} = exp(-\pi u^2)\,, \tag{2.66}$$

and

$$F\{f(ax)\} = \frac{1}{a} F\left(\frac{u}{a}\right) \ . \tag{2.67}$$

Using Equations (2.64) - (2.67) allows calculating Equation (2.63) as,

$$I = \sqrt{2\pi}\, exp(t^2)\, exp\left(-\frac{\xi^2}{2}\right) exp(-i2t\xi). \tag{2.68}$$

To use the result given by Equation (2.68) we now define $t = is$, thus, Equation (2.68) becomes,

$$\begin{aligned} I &= \sqrt{2\pi} exp\left(-\frac{\xi^2}{2}\right) exp(2\xi s - s^2) \\ &= \sum_{n=0}^{\infty} \left(\frac{(is)^n}{n!}\right) \int_{-\infty}^{\infty} H_n(x) exp\left(-\frac{x^2}{2}\right) exp(-ix\xi) dx \ . \end{aligned} \tag{2.69}$$

Using the generator function Equation (2.56) for the Hermite polynomials,

$$exp(2\xi s - s^2) = \textstyle\sum_{n=0}^{\infty} H_n(\xi)\ \left(\frac{s^n}{n!}\right), \tag{2.70}$$

Allows rewriting Equation (2.69) as

$$\begin{aligned} I &= \sqrt{2\pi} exp\left(-\frac{\xi^2}{2}\right) \sum_{n=0}^{\infty} H_n(\xi)\ \left(\frac{s^n}{n!}\right) \\ &= \sum_{n=0}^{\infty} i^n \left(\frac{s^n}{n!}\right) \int_{-\infty}^{\infty} H_n(x) exp\left(-\frac{x^2}{2}\right) exp(-ix\xi) dx \, . \end{aligned} \tag{2.71}$$

Using Equation (2.71) we obtain,

$$I = (-i)^n \sqrt{2\pi} exp\left(-\frac{\xi^2}{2}\right) H_n(\xi) \ = \int_{-\infty}^{\infty} H_n(x)\, exp\left(-\frac{x^2}{2}\right) exp(-ix\xi)\, dx \ .$$

(2.72)

In Equation (2.72), by making $\sigma = (-i)^n\sqrt{2\pi}$, allows writing the Fourier transform of the Hermite polynomials as,

$$\int_{-\infty}^{\infty} H_n(x)\, exp\left(-\frac{x^2}{2}\right) exp(-ix\xi)\, dx = \sigma H_n(\xi) exp\left(-\frac{\xi^2}{2}\right) . \tag{2.73}$$

This result will be helpful for the description of the following section.

2.4.2 Modes in a confocal resonator

There are many types of resonators, probably the most used to produce laser emission is the confocal resonator [25]. This resonator consists of a pair of concave mirrors $M1$, $M2$, of an equal radius of curvatures R , which are separated by a distance equal to the radius of curvature R, as depicted in Fig.(2.5). We will show that in such a structure, the transverse modes are Hermite-Gaussian distributions, being the lower mode a pure Gaussian field. Usually, a He-Ne laser is made to oscillate in this lower mode.

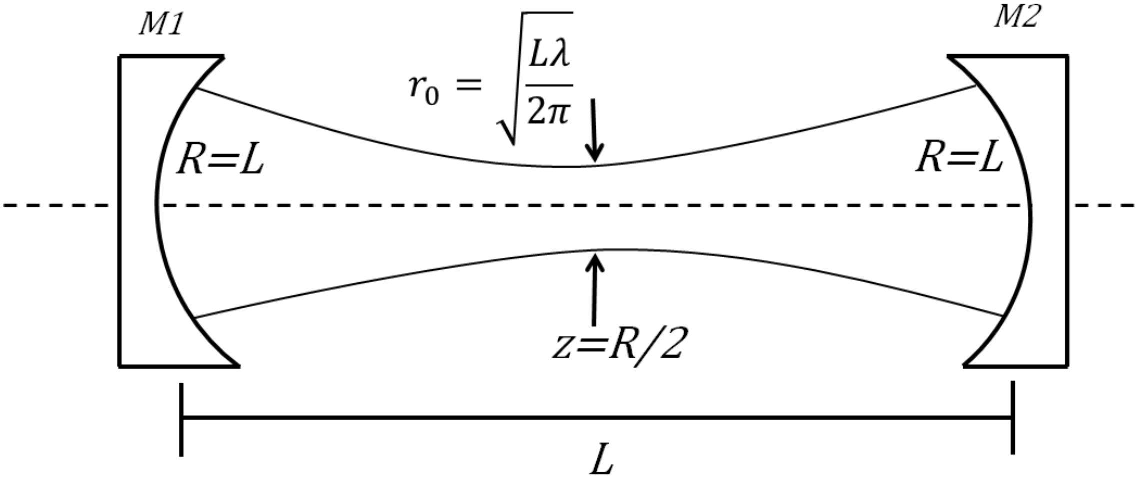

Fig. 2.5. Confocal resonator.

We will denote as $\psi(x)$ to the amplitude distribution at an initial plane with x coordinate. This field propagates along the confocal resonator until it bounces off the front mirror $M2$ located at a distance $z = R$ at a plane of observation with coordinate ξ. Thus, at the initial plane, the propagation integral that corresponds to the field distribution that bounces off the mirror is multiplied by a quadratic phase factor due to the reflection, that is, by a phase shift term of the form $exp\left(-\frac{i4\pi}{\lambda}h(\xi)\right)$, where $h(\xi)$ is the superficial distribution of the mirror $M2$ given by

$$h(\xi) = \frac{\xi^2}{2R}. \tag{2.74}$$

Thus, the phase shift due to the mirror reflection at the plane with coordinates ξ is,

$$exp\left(-\frac{i2\pi}{\lambda R}\xi^2\right). \tag{2.75}$$

The field distribution reflected for the mirror $M2$ at the plane in ξ, due to Equation (2.75) is written as,

$$\psi_R(\xi) = f(\xi)exp\left(-\frac{i2\pi}{\lambda R}\xi^2\right). \tag{2.76}$$

In Equation (2.76) $f(\xi)$ represents the initial field $\psi(x)$ propagated at a distance $z = R$. Using the Fresnel diffraction integral $f(\xi)$ can be expressed as

$$f(\xi) = \int_{-\infty}^{\infty} \frac{exp(ikR)}{\sqrt{ikR}} \psi(x)\, exp\left(\frac{i\pi}{\lambda R}(x-\xi)^2\right) dx\,. \tag{2.77}$$

Substituting $f(\xi)$ in the field reflected $\psi_R(\xi)$ by mirror $M2$, Equation (2.76) becomes,

$$\psi_R(\xi) = \left(\int_{-\infty}^{\infty} \frac{exp(ikR)}{\sqrt{ikR}} \psi(x)\, exp\left(\frac{i\pi}{\lambda R}(x-\xi)^2\right) dx\right) exp\left(-\frac{i2\pi}{\lambda R}\xi^2\right). \tag{2.78}$$

The Fresnel diffraction integral given by Equation (2.78) shows an operator acting on the initial amplitude distribution. After applying the propagation integral, the final amplitude distribution $\psi_R(\xi)$ can be obtained.

Thus, there exist a set of mathematical eigenmodes $\psi_n(x)$ and a corresponding set of eigenvalues σ_n such that each one of these eigenmodes after one round trip satisfies the round-trip propagation expression

$$\psi_n(x) = \sigma_n \psi(x)\,. \tag{2.79}$$

Equation (2.79) is called the resonator condition [27, 28] and establishes that after completing a round trip (a period) the field propagated must repeat itself at the selected reference plane, that in our case is the plane located at the ξ coordinate. Then, Equation (2.78) is written as

$$\psi(\xi) = \left\{\int_{-\infty}^{\infty} \frac{exp(ikR)}{\sqrt{ikR}} \psi(x)\, exp\left(\frac{i\pi}{\lambda R}(x-\xi)^2\right) dx\right\} exp\left(-\frac{i2\pi}{\lambda R}\xi^2\right) = \sigma_0 \psi(\xi)\,. \tag{2.80}$$

We now introduce the parameter σ_1 as,

$$\sigma_1 = \frac{exp(ikR)}{\sqrt{ikR}} \sigma_0, \tag{2.81}$$

Using the parameter defined in Equation (2.81) and by expanding the square term in Equation (2.80) we obtain,

$$\sigma_1 \psi(\xi) exp\left(\frac{i\pi}{\lambda R} \xi^2\right) = \int_{-\infty}^{\infty} \psi(x)\, exp\left(\frac{i\pi}{\lambda R} x^2\right) \exp\left(-\frac{i2\pi}{\lambda R} x\xi\right) dx\,. \tag{2.82}$$

The limits in the integral in Equation (2.82) are extended from $-\infty, \infty$ as the size of the beam width is small compared with the size of the mirrors.

In the integral of Equation (2.82), we define the following variables,

$$\frac{\pi}{\lambda R} x^2 = \frac{s^2}{2}, \tag{2.83}$$

$$\frac{2\pi}{\lambda R} x\xi = sv, \tag{2.84}$$

and,

$$\sqrt{\frac{2\pi}{\lambda R}} x = s. \tag{2.85}$$

Then, the values of x , ξ, and the product $x\xi$ in Equations (2.83 - 2.85) become,

$$\sqrt{\frac{2\pi}{\lambda R}} \xi = v, \tag{2.86}$$

$$x = \sqrt{\frac{\lambda R}{2\pi}} s, \tag{2.87}$$

$$\xi = \sqrt{\frac{\lambda R}{2\pi}} v, \tag{2.88}$$

$$x\xi = \frac{\lambda R}{2\pi} sv. \tag{2.89}$$

Substituting the changes of variables given by the Equations (2.83 - 2.89), in Equation (2.82) give,

$$\sigma_2 \psi(v) exp\left(\frac{iv^2}{2}\right) = \int_{-\infty}^{\infty} \psi(s)\ exp\left(\frac{is^2}{2}\right) \exp\ (-isv) ds\ . \tag{2.90}$$

It is necessary to rewrite the Equation (2.90), for this, let,

$$u(s) = \psi(s)\ exp\left(\frac{is^2}{2}\right), \tag{2.91}$$

and

$$u(v) = \psi(v)\ exp\left(\frac{iv^2}{2}\right). \tag{2.92}$$

Using Equations (2.91) and (2.92) allows rewriting Equation (2.90) as,

$$\sigma_2 u(v) = \int_{-\infty}^{\infty} u(s) \exp(-isv) ds\ . \tag{2.93}$$

Comparing Equation (2.93) with the Fourier Hermite transform given by Equation (2.73) gives,

$$exp\left(-\frac{v^2}{2}\right) \sigma H_n(v) = \int_{-\infty}^{\infty} H_n(s)\ exp\left(-\frac{s^2}{2}\right) \exp\ (-isv) ds\, . \tag{2.94}$$

Equation (2.94) implies that,

$$u(s) = H_n(s)\ exp\left(-\frac{s^2}{2}\right). \tag{2.95}$$

From Equation (2.95) it follows that,

$$u(s) = \psi(s)\ exp\left(\frac{is^2}{2}\right) = H_n(s)\ exp\left(-\frac{s^2}{2}\right). \tag{2.96}$$

Equation (2.96) indicates that $\psi(s)$ must be,

$$\psi_n(s) \; = H_n(s) \, exp\left(-\frac{s^2}{2}\right) exp\left(-\frac{is^2}{2}\right). \tag{2.97}$$

Now substituting in $\psi_n(s)$ the value of s given by Equation (2.85), Equation (2.97) becomes,

$$\psi_n(s) \; = H_n\left(\sqrt{\frac{2\pi}{\lambda R}}x\right) exp\left(-\frac{\pi x^2}{\lambda R}\right) exp\left(-i\frac{\pi x^2}{\lambda R}\right). \tag{2.98}$$

The solutions given by Equation (2.98) are the modes of propagation in the resonator. The result can be generalized to a two-dimensional resonator. In two dimensions these Gaussian modes are characterized by different values of m and n and are referred to as transverse electromagnetic modes of order (m,n) or TEM_{mn} modes, because of their different intensity transverse patterns. Some TEM_{mn} intensity modes are depicted in Fig.(2.6).

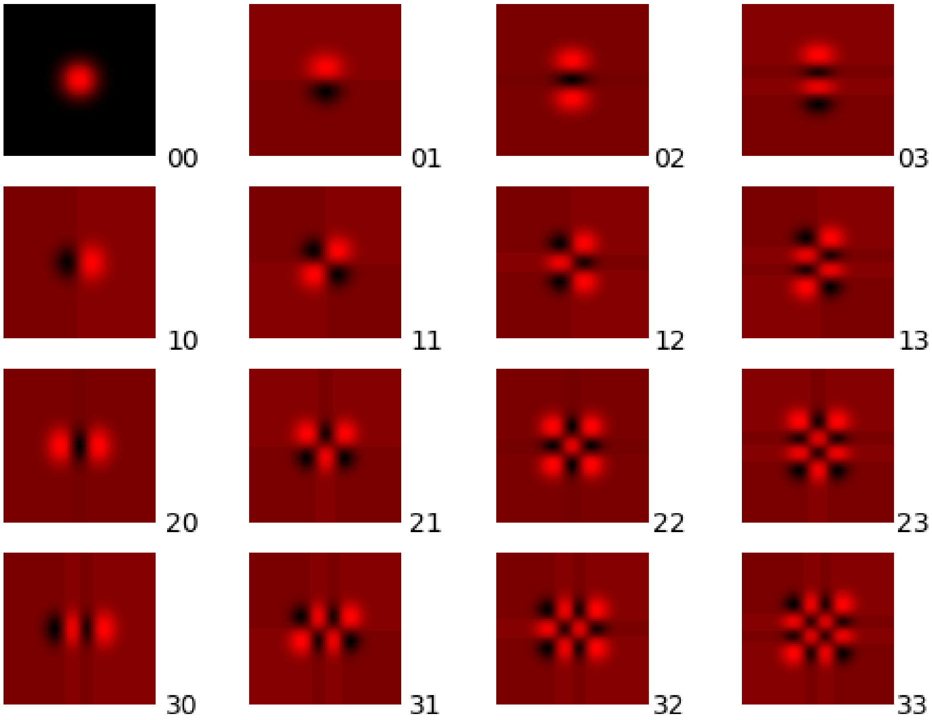

Fig. 2.6. Transverse modes TEM_{mn}.

In the special one-dimensional case, $n = 0$, we obtain the zero-order Gaussian mode $\psi_0(s)$ as,

$$\psi_0(s) = H_0\left(\sqrt{\frac{2\pi}{\lambda R}}\,x\right) exp\left(-\frac{\pi x^2}{\lambda R}\right) exp\left(-i\frac{\pi x^2}{\lambda R}\right). \tag{2.99}$$

In Equation (2.99), H_0 is equal to one, then we can write the zero-order Gaussian modes as

$$\psi_0(x) = exp\left(-\frac{\pi x^2}{\lambda R}\right) exp\left(-i\frac{\pi x^2}{\lambda R}\right). \tag{2.100}$$

To see where the field focuses, we propagate the field ψ_0, given by the Equation (2.100) up to a distance $z = R/2$ which represents the middle distance of the resonator length, then we have,

$$\psi(\xi) = \int_{-\infty}^{\infty} exp\left(-\frac{\pi x^2}{\lambda R}\right) exp\left(-i\frac{\pi x^2}{\lambda R}\right) exp\left(\frac{i\pi}{\lambda\left(\frac{R}{2}\right)}(x-\xi)^2\right) dx\ . \tag{2.101}$$

Expanding the square binomial in the integral given in the Equation (2.101), and factorizing some terms, we obtain

$$\psi(\xi) = exp\left(\frac{i2\pi}{\lambda R}\xi^2\right) \int_{-\infty}^{\infty} exp\left(-\pi\frac{(1-i)}{\lambda R}x^2\right) exp\left(-i2\pi x\left(\frac{2\xi}{\lambda R}\right)\right) dx\,. \tag{2.102}$$

Equation (2.102) can be solved using the Fourier transform properties given by Equations (2.66 - 2.67). Then the Fourier transform in Equation (2.102) is given as,

$$\int_{-\infty}^{\infty} exp\left(-\pi\frac{(1-i)}{\lambda R}x^2\right) exp\left(-i2\pi x\left(\frac{2\xi}{\lambda R}\right)\right) dx = exp\left(-\pi\frac{\lambda R}{(1-i)}\left(\frac{2\xi}{\lambda R}\right)^2\right). \tag{2.103}$$

Using Equation (2.103) allows writing the solution for $\psi(\xi)$ given by Equation (2.102) as

$$\psi(\xi) = exp\left(\frac{i2\pi}{\lambda R}\xi^2\right) exp\left(-\pi\frac{(1+i)}{2\lambda R}4\xi^2\right). \tag{2.104}$$

Equation (2. 104) can be simplified as,

$$\psi(\xi) = exp\left(-\frac{\xi^2}{{r_0}^2}\right). \tag{2.105}$$

The Equation (2.105) represents a Gaussian function. That is, the propagated field $\psi_0(s)$ is focused in the middle of the resonator $z = R/2$ with a semi-width r_0 given by

$$r_0 = \sqrt{\frac{\lambda R}{2\pi}}\ . \tag{2.106}$$

The Fig.(2.7) depicts the normalized intensity of this particular case of a zero-order Gaussian beam in a confocal resonator, focused at $z = R/2$ with a semi-width r_0 given by the Equation (2.106). This is the case for a He-Ne laser.

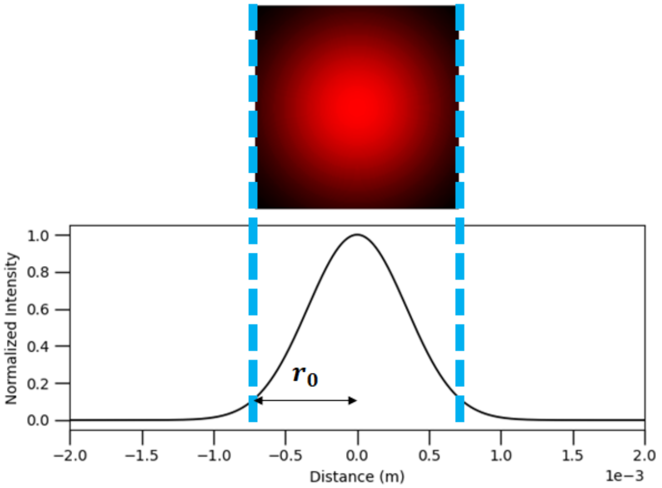

Fig. 2.7. Zero-order Gaussian beam in a confocal resonator.

Using the Equation (2.106), we can obtain the change in the semi-width of this zero-order Gaussian beam as

$$dr_0 = \frac{1}{2}\sqrt{\frac{\lambda}{2\pi}}\ \frac{dR}{\sqrt{R}}. \qquad (2.107)$$

Equation (2.107) reveals that, for practical purposes, the standing wave pattern stays fixed during the reflections inside the resonator. Equivalently, for a commercially available He-Ne laser, changes of the beam width can be neglected as otherwise, if the value of Equation (2.107) would increase, the resonator could not continue attaining the output beam.

Nevertheless, temperature and minor misalignments could cause small losses in power but not any appreciable change in the semi-width of the beam.

In the next section, we will describe a numerical method to propagate the Gaussian beam through the optical system.

2.5 Fresnel Gaussian Shape Invariant (FGSI)

It is possible to calculate analytically the intensity profile at the observation plane by using a numerical method referred to as the Fresnel Gaussian shape invariant (FGSI). This method is based on a finite superposition of Gaussian wavelets for representing an arbitrary complex wave-front [18-21]. Thus, the process of propagation of the illuminating Gaussian beam will be carried out by iterative application of the equations of the FGSI method from the initial plane to the lens, through the sample under test up to the observation plane. The equations of the method are the following.

The amplitude distribution of each Gaussian wavelet at a given nth-plane is represented as

$$\Psi_n(x) = P_n exp(i\alpha_n x) exp(i\beta_n x^2) exp\left(-\frac{(x-A_n)^2}{r_n^2}\right) exp(i\gamma_n (x-B_n)^2). \tag{2.108}$$

In Equation (2.108) the Gaussian distribution is spatially centered at A_n and P_n is a complex constant term that represents the amplitude of the Gaussian beam. The parameter α_n represents a tilt of the beam, and β_n is introduced to allow an arbitrary defocusing quadratic phase. Here, γ_n is the factor that represents the Gaussian curvature whose quadratic phase is centered at B_n. In general, both centers do not coincide.

The amplitude distribution with wavelength λ, represented by Equation (2.108) at the initial plane, is propagated a distance z, up to an observation plane with coordinate x_F. The iterative equations required to propagate this field by FGSI are obtained employing the Fresnel diffraction integral [22]. After performing the integral, the amplitude distribution at this plane is given by

$$\begin{aligned}\Psi_{n+1}(x_F, z) = {} & P_{n+1} exp(i\alpha_{n+1} x_F) exp(i\beta_{n+1} {x_F}^2) \\ & \times exp\left(-\frac{(x_F - A_{n+1})^2}{r_{n+1}^2}\right) exp(i\gamma_{n+1}(x_F - B_{n+1})^2) \ ,\end{aligned} \tag{2.109}$$

where,

$$\begin{aligned}P_{n+1} = P_n \frac{exp\left(\frac{i2\pi z}{\lambda}\right)}{\sqrt{i\lambda z}} \sqrt{\frac{\pi r_n^2 \lambda z}{\lambda z - i r_n^2(\beta_n \lambda z + \gamma_n \lambda z + \pi)}} \times \\ exp(i\gamma_n B_n^2) exp\left(i \frac{\lambda z A_n^2}{r_n^4(\beta_n \lambda z + \gamma_n \lambda z + \pi)}\right),\end{aligned} \tag{2.110}$$

and,

$$\alpha_{n+1} = 0, \quad \beta_{n+1} = \frac{\pi}{\lambda z}, \quad \gamma_{n+1} = \frac{\pi^2 r_n^4}{D_n \lambda z}(\beta_n \lambda z + \gamma_n \lambda z + \pi) \, , \tag{2.111}$$

$$r_{n+1} = \frac{\sqrt{D_n}}{\pi r_n}, \tag{2.112}$$

$$A_{n+1} = A_n + \frac{\alpha_n \lambda z}{2\pi} - \frac{\gamma_n \lambda z B_n}{\pi} + \frac{(\beta_n + \gamma_n)\lambda z A_n}{\pi} , \tag{2.113}$$

$$B_{n+1} = \frac{\alpha_n \lambda z}{2\pi} - \frac{\gamma_n \lambda z B_n}{\pi} - \frac{\lambda^2 z^2}{\beta_n \lambda z + \gamma_n \lambda z + \pi} \frac{A_n}{\pi r_n^4} , \tag{2.114}$$

For brevity in Equation (2.5.4) and Equation (2.5.5) the term D_n is defined as

$$D_n = \lambda^2 z^2 + r_n^4 (\beta_n \lambda z + \gamma_n \lambda z + \pi)^2. \tag{2.115}$$

The set of Equations (2.111-2.112) is iteratively applied at each interface of the optical setup. The entrance angle θ, the wavelength λ, and the refractive index n have to be updated at each interface according to the corresponding iteration. This task will be performed using the following equations

$$\lambda = \frac{\lambda_0}{n}, \tag{2 .116}$$

$$\alpha_n = \frac{2\pi}{\lambda} tan(\theta) + 2\gamma_n B_n - 2(\beta_n + \gamma_n) A_n , \tag{2.117}$$

$$P_n = P_n \, exp(-i\alpha_n A_n) , \tag{2.118}$$

λ_0 in Equation (2.116) represents the wavelength of the illuminating beam in free space. The appropriate tilt at each corresponding interface is established by the above equations.

At the front surface of the lens in which the beam under propagation changes its curvature R to allow a convergent or diverging wave-front, the term β_n and P_n will be replaced by the new relations

$$\beta_n = \beta_n - \frac{\pi \, (n_2 - n_1)}{\lambda \, R}, \tag{2.119}$$

$$P_n = P_n exp\left(i\frac{\pi\,(n_2 - n_1)}{\lambda\, R}\,(A_n)^2\right).$$

(2.120)

In Equations (2.119-2.120) n_2 is the index of refraction of the lens and n_1 is the index of refraction of the free space. These equations must be used together to maintain the corresponding FGSI continuous at the interface.

The intensity profile at the observation plane is calculated utilizing FGSI. Additionally, this profile is experimentally recorded with high resolution by using a homodyne detector specially designed for this task. Both profiles, the analytical and the experimental are compared to guarantee the correctness of the results. The homodyne detector is described in the next section.

2.6 Homodyne detector

Our especially dedicated homodyne detector, depicted in Fig.(2.8), consists of a photodiode whose sensitive area is much larger than the dimensions of the recorded beam placed behind a vibrating knife-edge. A flexure mode piezoelectric transducer (PZT) is used to vibrate the knife-edge at a low frequency (ν), transversally to the optical axis. The oscillation signal is provided by a lock-in amplifier which also receives the output signal photodiode signal. A flexure mode PZT is used because it exhibits a low tilt (less than 5μrad for a total displacement of 100μm) and a positioning resolution of about 2nm. This resolution is adequate compared with the displacement steps required to record the intensity profiles at the plane of observation with high resolution.

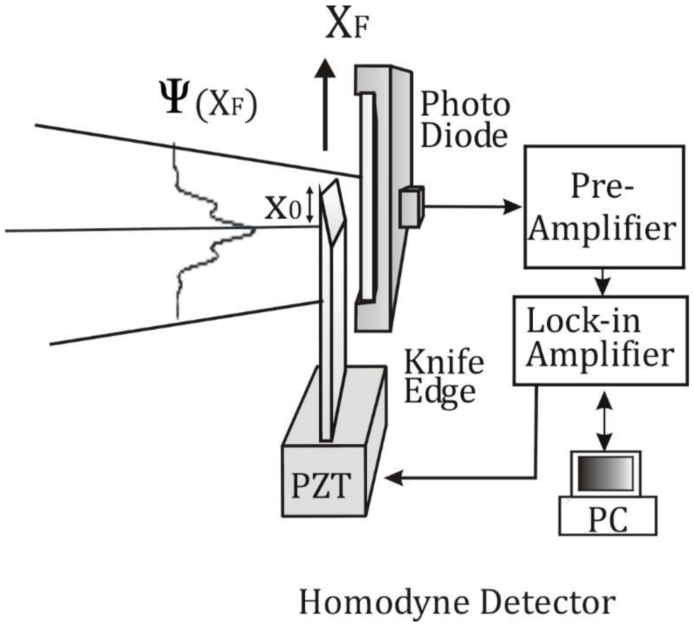

Fig.2.8. Homodyne detector.

The photodiode is partially blocked by a knife-edge. Thus, the recorded power, P, can analytically be expressed as,

$$P = \sqrt{\frac{2{P_0}^2}{\pi r_0^2}} \int_{x(t)}^{\infty} exp\left(-2\frac{x^2}{r_0^2}\right) dx \, . \tag{2.121}$$

In Equation (2.121) P_0 represents the beam power, r_0 the semi-width of the laser beam at the initial plane, and $x(t)$ represents the position blocked by the knife-edge whose position as a function of time t can be expressed as

$$x(t) = \frac{\sqrt{2}}{r_0}(x_0 + \delta_0 \cos(\, 2\pi v t)) \, . \tag{2.122}$$

In the Equation (2.122), x_0 represents the initial position of the edge of the knife and $\delta_0 \sim 1\mu$ represents a small amplitude.

We now make a change of variable in the integral given by Equation (2.121) as,

$$u = \frac{\sqrt{2}}{r_0} x \,. \tag{2.123}$$

Using Equation (2.122) allows rewriting Equation (2.121) as,

$$P = \frac{2}{\sqrt{\pi}} \sqrt{\frac{2{P_0}^2}{\pi r_0^2}} \int_{x(t)}^{\infty} exp(-u^2)\, du = B\mathrm{erfc}\left(\frac{\sqrt{2}}{r_0} (x_0 + \delta_0 \cos(\, 2\pi v t)) \right) . \tag{2.124}$$

In Equation (2.124), as the value δ_0 is small, we calculate a Taylor series expansion as,

$$P = B\left(\mathrm{erfc}\left(\frac{\sqrt{2}}{r_0} x_0 \right) + \frac{d}{dx}\left(\mathrm{erfc}\left(\frac{\sqrt{2}}{r_0} x_0 \right) \frac{\sqrt{2}}{r_0} \delta_0 \cos(\, 2\pi v t) \right) \right). \tag{2.125}$$

In Equation (2.125), we have used,

$$\frac{d}{dx} \mathrm{erfc}(x) = \frac{2}{\sqrt{\pi}} exp(-x^2) \,. \tag{2.126}$$

Now, the power P, given by the Equation (2.125) becomes a function of x_0. Then, Equation (2.125) is rewritten as,

$$P(x_0) = B\; exp\left(-2 \frac{x_0^2}{r_0^2} \right) \cos(2\pi v t) \,. \tag{2.127}$$

In Equation (2.127) the amplitude B includes all the constant terms.

Equation (2.127) gives the power recorded by the photodiode. An output signal, proportional to $P(x_0)$ is then obtained at the output of the photodiode and it is amplified by a "lock-in" which filters undesired noise. The intensity profile is obtained by displacing the knife-edge to different values x_0 along the region of the beam. The high precision of this detector allows recording appropriately the intensity profiles under study.

In the following section, we present experimental results.

3. Application for glucose concentration measurements

Measuring glucose concentration with high accuracy and repeatability is highly important for monitoring glucose levels in persons with diabetes and other diseases as without appropriate detection and treatment could result in serious health implications [29]. It is possible to measure glucose concentration by chemical testing; however, the main limitation relies on that the chemical substances used can react with other constituents besides glucose [30].

New optical techniques have been studied [31], but in general, the main limitation is that the signal obtained from the optical systems, in general, overlaps the signal of other constituents due to low signal to noise ratios, thus, requiring additional processing and data analysis intending to attain reliable results [30, 31, 32]. Our new optical approach overcomes this limitation as illustrated in the following sections.

3.1 Theoretical glucose measurements

According to the sensitivity requirements, the system can be used in one of two modes. Both modes use a high-aberrated probe beam to measure the changes in the concentration. Fig. (3.1) depicts the low sensitivity optical setup. In its first mode of operation, referred here as the low sensitivity mode, the system is intended for glucose concentrations in steps of 100 mg/dl or higher. Without loss of generality, the low sensitivity mode will be used in this section to demonstrate how a high-aberrated probe beam improves the sensitivity compared with a previous optical technique based on the diffractive characteristics of a Gaussian beam free of aberrations [33]. The low sensitivity mode may be useful in several fields of industry, as, in the food industry.

As mentioned above a one-dimensional description will find to be sufficient for our description.

The illuminating beam is a He-Ne laser with wavelength λ = 632.8 nm and Gaussian amplitude distribution $\Psi(x)$, placed at an initial plane with coordinate x. At a distance z_0 from the initial plane, the vertex of a singlet focusing lens is positioned. The observation plane with coordinate x_F is located at a distance z_1 from the back surface of the lens. The amplitude distribution at the observation plane is represented as $\Psi_F(x_F)$. A sample with width w is placed between the lens and the observation plane and its exact position becomes irrelevant. Due to the divergence of the Gaussian beam the semi-width of the beam increases as the distance of propagation increase, thus, to achieve a high-aberrated probe beam it is necessary to choose an appropriated z_0 distance to illuminate a large area of the spherical front surface of the lens but at the same time avoiding visible truncation of the beam. On the other hand, if a Gaussian probe beam free of aberrations should be required, then, a small area of the lens should be illuminated.

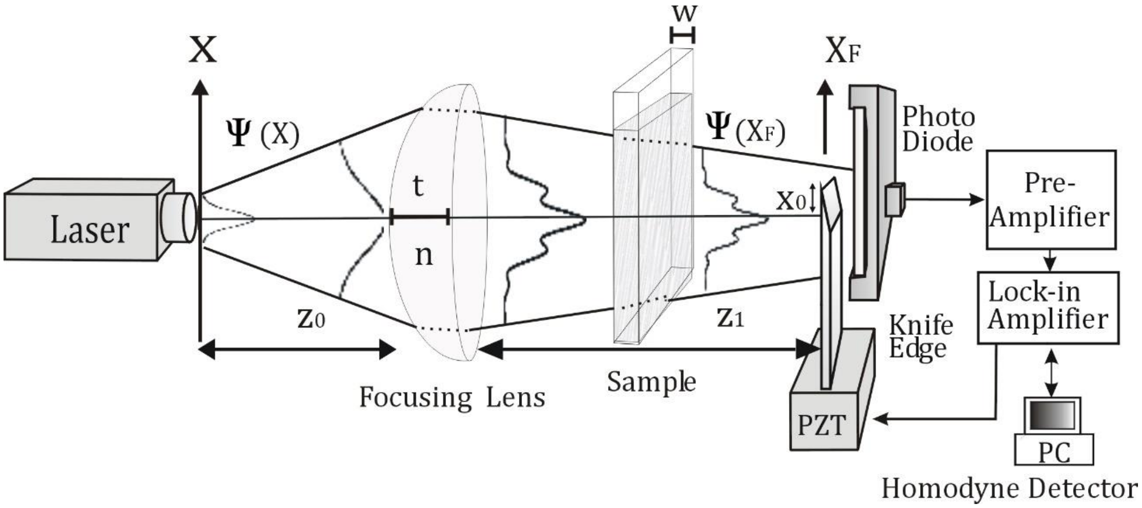

Fig. 3.1. Optical setup for measuring changes of concentration for the low sensitivity model. The vertex of a singlet focusing lens is placed at a distance z_0 from the waist-plane with a coordinate$x$of an illuminating laser Gaussian beam. The observation plane with coordinate x_F is located at a distance z_1 from the back surface of the lens of central thick t. The sample with width w is placed as described in the text.

For comparison purposes, it is necessary to perform the calculations of the propagation of the high-aberrated Gaussian beam and also the propagation of the Gaussian beam free of aberrations through the experimental setup depicted in Fig.(3.1). For this purpose, we use the numerical FGSI method. With the results obtained, we will be able to compare the sensitivity of both optical stems when changes in the index of refraction of the sample under test occur.

For the task described above, we now calculate the normalized intensity distributions at the observation plane for z_0 = 1 m and 5 m, varying in each case the index of refraction of the sample into five different values, n = 1.330, 1.333, 1.336, 1.339 and 1.342. The first value n = 1.330 corresponds approximately to the index of refraction of pure tri-distilled water, or equivalently, it corresponds to a sample with a glucose concentration of 0 mg/dl. The distance z_1 was fixed at approximately 26 mm which corresponds to the best focusing conditions of our lens. The corresponding normalized intensity profiles at the plane of observation are depicted in Fig.(3.2).

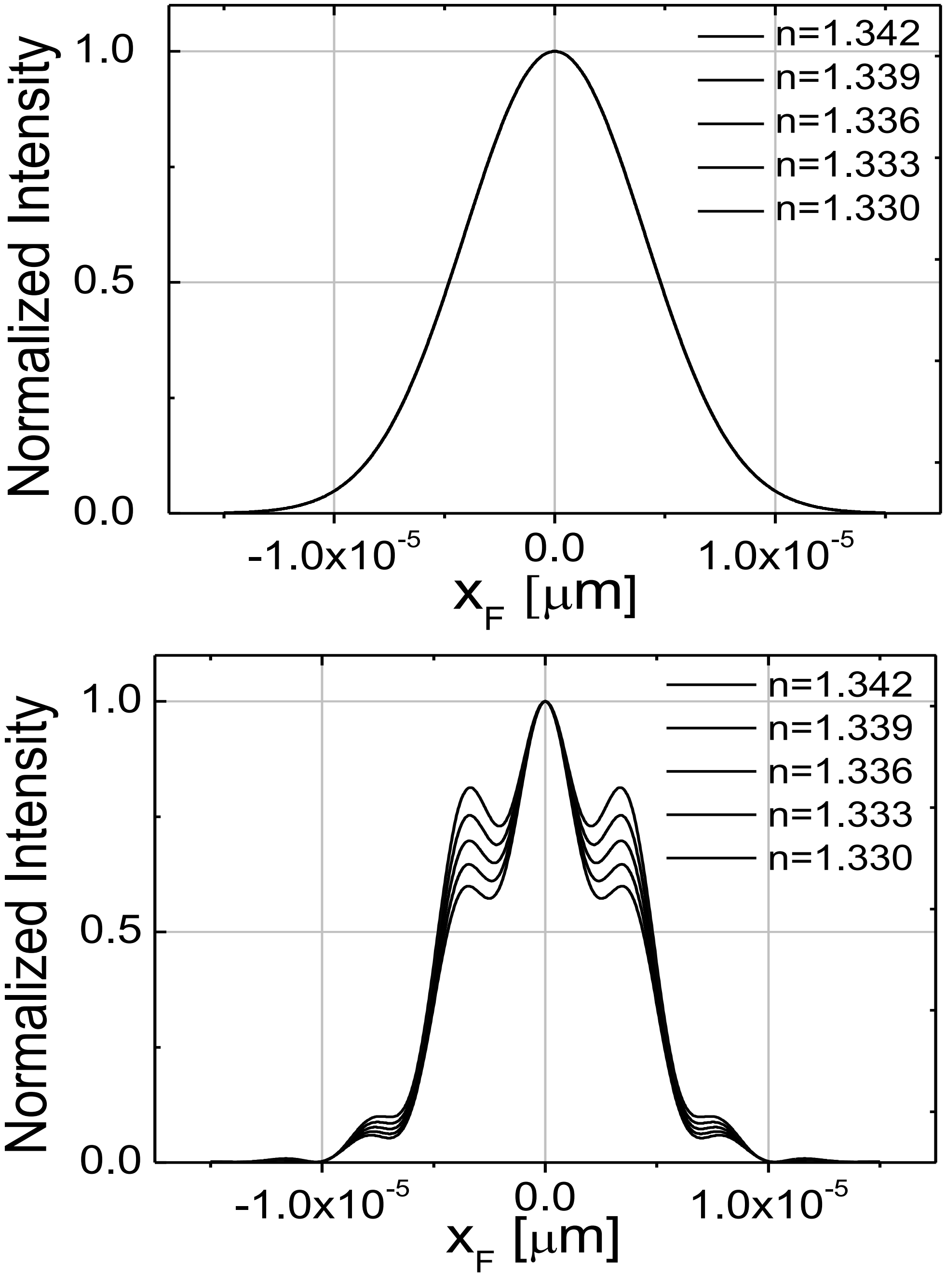

Fig. 3.2. Analytical normalized intensity distributions calculated by FGSI. Normalized intensity distributions at the observation plane for different indexes of refraction in the sample. a) corresponds to z_0= 1 m and b) to z_0=5 m; z_1~ 26 mm.

For the first case the distance z_0 has been set to 1.0 m. In this case, the laser beam is not very far from the lens as revealed by Fig.(3.2a) which exhibits an intensity Gaussian distribution visually free of aberration. In contrast, for the second case, when the distance z_0 is set to 5.0 m, Fig.(3.2b) reveals that the intensity profiles exhibit side-lobes at each side of the central peak. This side- lobes correspond to spherical aberrations and are the result of illuminating a higher region of the front surface of the lens. It can be observed that changing the index of refraction n of the sample, for the Gaussian free aberration case, does not result in any appreciable changes in their corresponding intensity profiles. In contrast, the intensity profiles of the aberrated case show notable changes in the heights of the side-lobes on the intensity normalized profiles.

The above result clearly demonstrates the usefulness of the side-lobes that are present in the aberrated case. However, in existing systems, some involuntary misalignments may occur. To calculate the effects of slight misalignments in experimental systems, we performed now similar calculations, but this time introducing intentionally some misalignments in our analytical model. The results obtained for this physical situation are depicted in Fig. (3.3). In these calculations, some misalignments were included for both cases, the aberrated and the free-aberrated one. For illustrative purposes, we have exaggerated a real situation by introducing an exaggerated misalignment to our analytical model. It can be appreciated in Fig. (3.3) that even with a severe misalignment of the optical components, for the aberrated case, the system maintains its high sensitivity, making this system useful even under difficult working conditions.

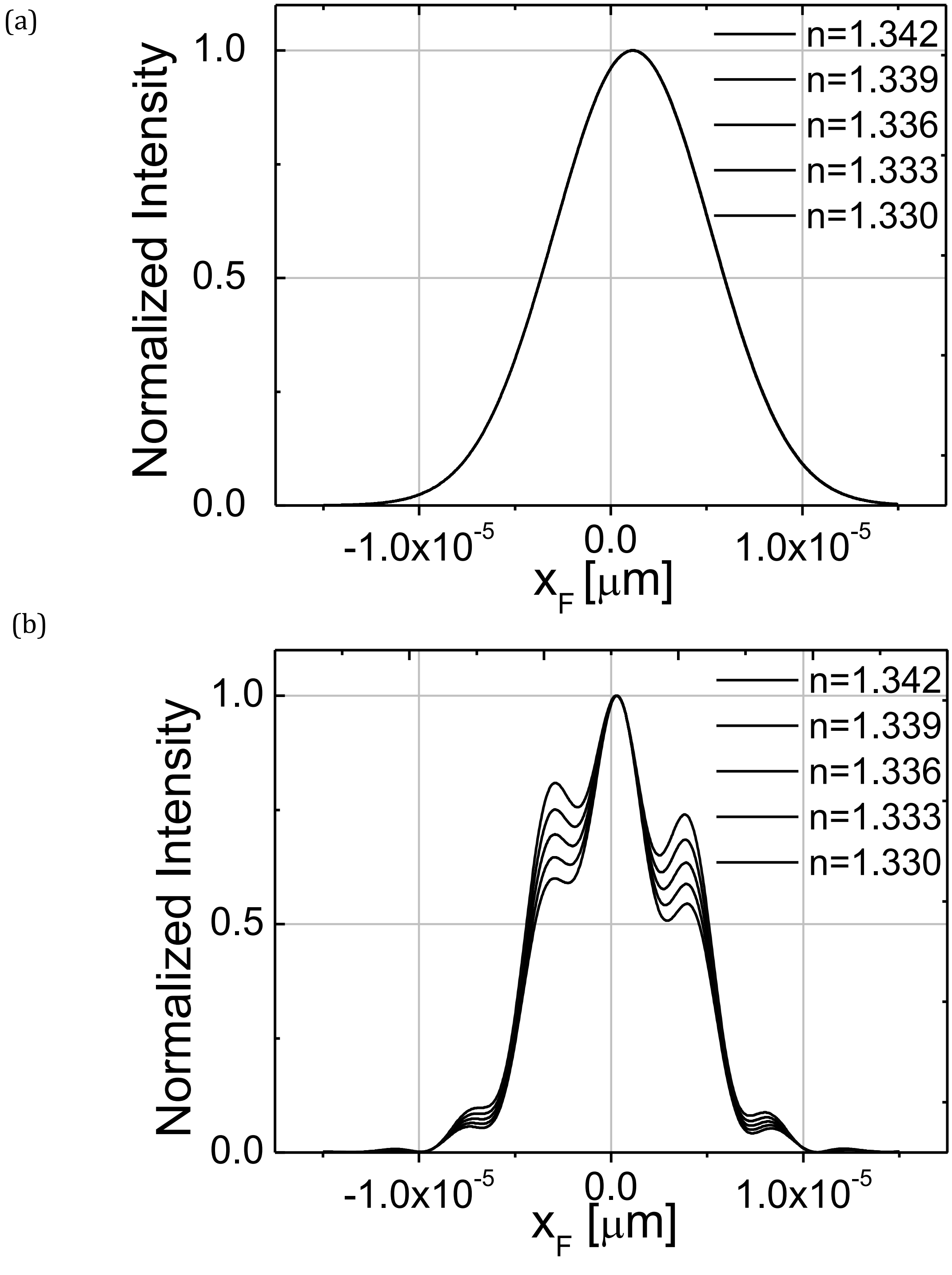

Fig. 3. 3. Analytical normalized intensity distributions calculated by FGSI with some misalignment. Normalized intensity distributions at the observation plane for different indexes of refraction in the sample when some misalignment is present in the system. (a) corresponds to z_0= 1 m and (b) z_0= 5 m; $z_1 \approx$ 26 mm.

Once that we have demonstrated that the heights of the primary side-lobes are highly sensitive to changes in the index of refraction, in the following section, we present our experimental results. Our experimental results will be compared with our analytical model based on the FGSI formulation.

3.2 Experimental glucose measurements

The illuminating source was a He-Ne laser, λ = 632 nm, with an output power of approximately 5 mW. As mentioned above, the power of the laser does not influence the measurements and can be chosen freely. The laser output has a beam diameter of $\frac{1}{e^2}$ =0.8 mm. For the low sensitivity mode, the plane-convex singlet focusing lens used in our set-up has a radius of curvature R = 1.552 cm, back focal length 2.79 cm, refractive index 1.517, central thickness t = 0.318 cm, and clear aperture 1.4 cm. The vertex of the lens was placed at a distance z_0= 5 m from the waist-plane of the laser, as depicted in Fig. (3.1). A cuvette contains the transparent liquid under inspection. The walls of the cuvette consist of glass with a thickness of 0.1= cm and it has an internal width w = 1 cm. The cuvette was positioned between the homodyne detector and the lens. The homodyne profiler described above has to be positioned at a distance z_1 from the back surface of the lens as depicted in Fig. (3.1). This distance is adjusted by mounting the profiler on a commercially available positioning stage. The stage is then moved forth and back to attain a distance z_1 that sets the maximum of the primary side-lobes at a desired height of the normalized intensity profile recorded. In our case, we set the height at 60% of the maximum of the normalized intensity profile when the sample corresponds to a concentration C_w= 0 mg/dl, as depicted in Fig.(3.4). It can be noticed from the intensity profiles that our experimental setup had a small misalignment that, as demonstrated above did not affect its sensitivity.

To calibrate the system, five different solutions on tri-distilled water were prepared. The corresponding glucose concentrations were, C_w= 0 mg/dl, C_1= 100 mg/dl, C_2= 200 mg/dl, C_3= 300 mg/dl and C_4= 400 mg/dl. For each measurement, the cuvette was filled with the corresponding solution. On replacing solutions, it is necessary to take care of maintaining unaltered the position of the optical components.

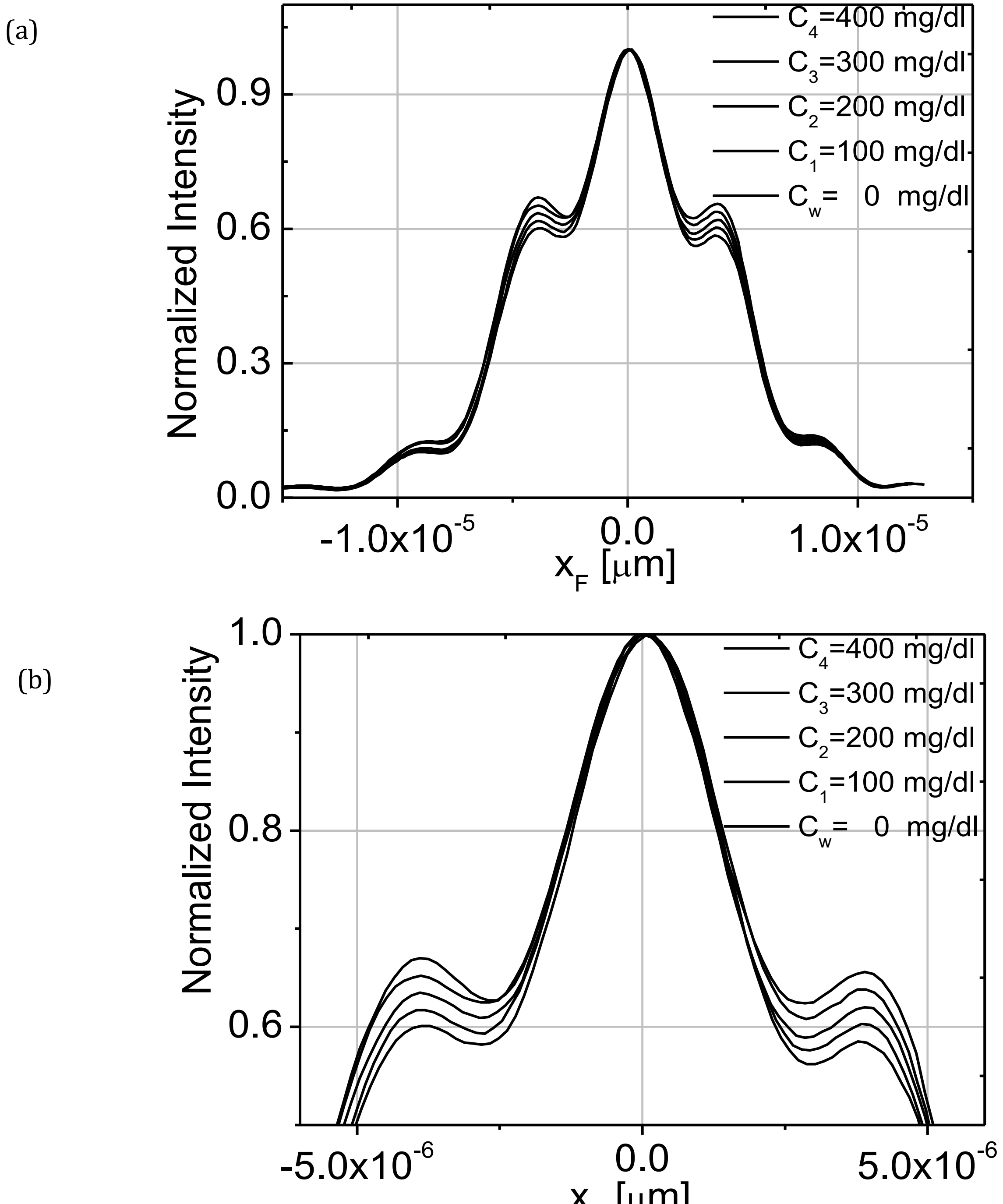

Fig. 3.4. Experimental normalized intensity distributions. (a) Experimental normalized intensity distributions at the observation plane for five glucose concentrations. C_w = 0 mg/dl and 100 mg/dl, 200 mg/dl, 300 mg/dl and 400 mg/dl. As glucose concentration increases the vertical height of the side-lobes increases. (b) Amplified view of the region of interest for better visualization.

Fig.(3.4) shows plots of the experimental results for the five concentrations described above. In Fig. (3.5). the maxima vertical heights of both primary side-lobes versus glucose concentrations are plotted. It can be noticed that the vertical heights of the primary side-lobes have a linear dependence with glucose concentration.

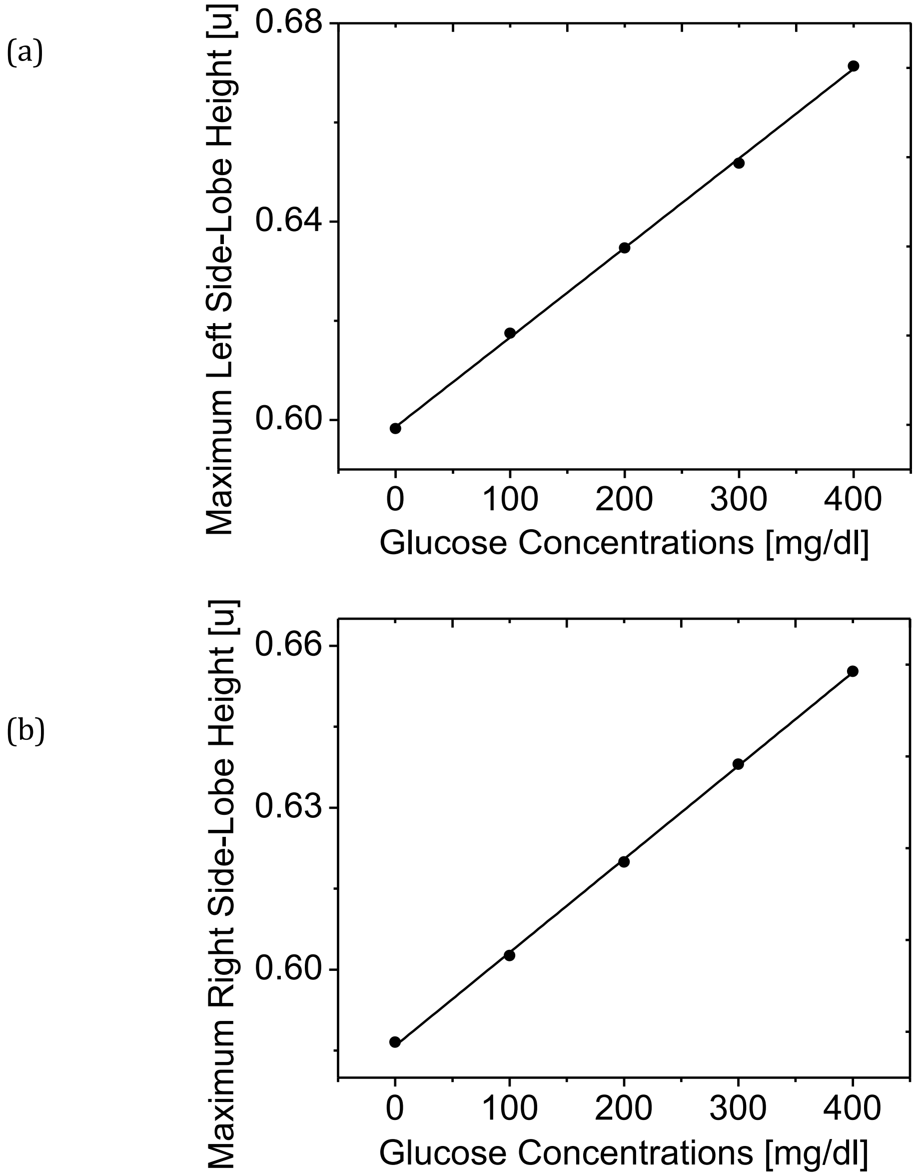

Fig. 3.5. Primary side-lobes heights as a function of glucose concentration. Plots of the maxima vertical heights for both primary side-lobes as a function of glucose concentration. (a) and (b) correspond to the left and right primary side-lobes respectively. Dots correspond to experimental values. Continuum lines correspond to linear fits.

From linear fits plotted in Fig.(3.5), the following linear Equations(3.1)-(3.2) for the left and right primary side-lobes are obtained as,

$$y_L = (1.806 \times 10^{-4})C + 0.599 \,, \tag{3.1}$$

$$y_R = (1.729 \times 10^{-4})C + 0.586 \,. \tag{3.2}$$

As both side-lobes exhibit a linear behavior, for glucose concentration measurement it is sufficient to focus on only one of the primary side-lobes.

The proposed technique can also be used with turbid samples. Although this subject is still under study, as a preliminary result in this direction, we measured the glucose concentration of a sample with a 0.2% concentration of evaporated milk in tri-distilled water. Fig.(3.6) shows that although the probe beam is highly scattered by the turbid media, the relative heights of the primary side-lobes can still be recorded accurately even under these conditions. This preliminary experiment is highly promising and it is presented here only for illustrative purposes.

(a)

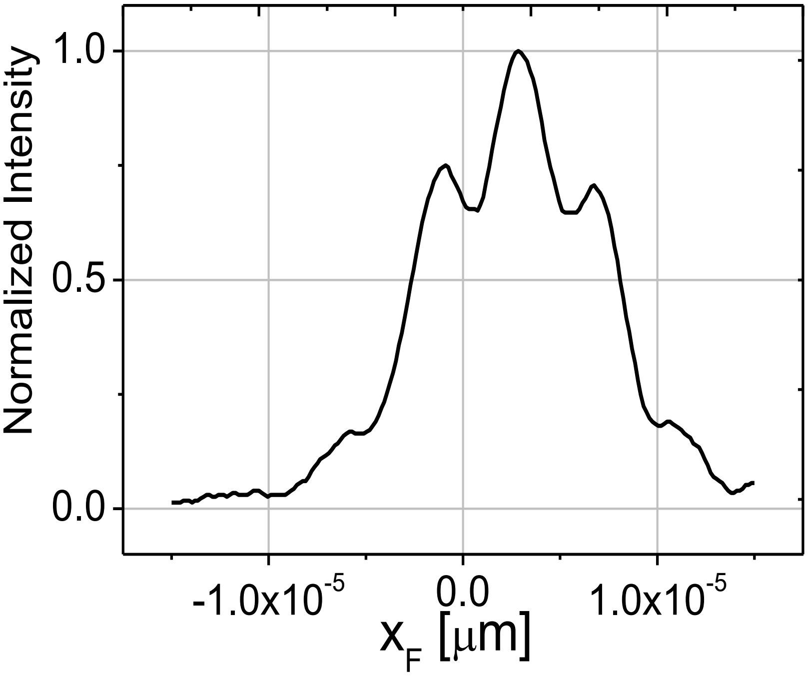

(b)

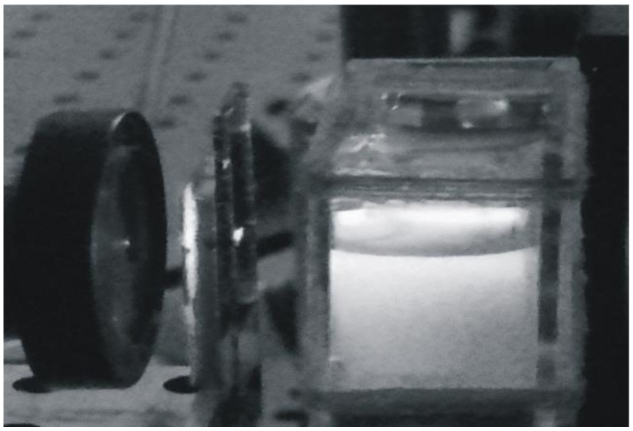

Fig. 3.6. Experimental normalized intensity distributions for a turbid sample. (a) Experimental normalized intensity distribution at the observation plane for a turbid sample as described in the text. (b) Photograph of the illuminating beam transmitted by the sample.

At this point, we have demonstrated that our low sensitivity model has a linear response and high repeatability, making this system feasible for glucose concentration measurements for relatively large concentrations. It is possible to increase the sensitivity to a range of clinical tests by replacing the lens from the optical setup by a lens-shaped container as described in the next section.

3.3 Theoretical glucose measurements replacing the lens by a singlet-lens-shaped container (SLSC)

Fig.(3.7) depicts the optical setup for our high sensitivity mode system, increasing the abovementioned sensitivity. The focusing lens is now replaced by a single-lens-shaped container (SLSC). Due to the divergence of the Gaussian beam, at z_0= 5m, the beam semi-width at the front surface of the SLSC is $r_0\sqrt{1+\frac{(\lambda z_0)^2}{(\pi^2 {r_0}^4)}}$ = 1.78 mm. The SLSC is made of BK7, with a radius of curvature R = 1.0 cm and internal width at its center of approximately t = 3.0 mm. The container is filled with the sample under test and for practical purposes, the illuminating beam path trajectory will correspond to the refractive index of this special singlet lens, being equal to the refractive index (n) of the sample. The observation plane is placed at a distance z_1 behind the SLSC and close to its back focal plane. The homodyne detector records the intensity profiles of the aberrated beam as in the above case.

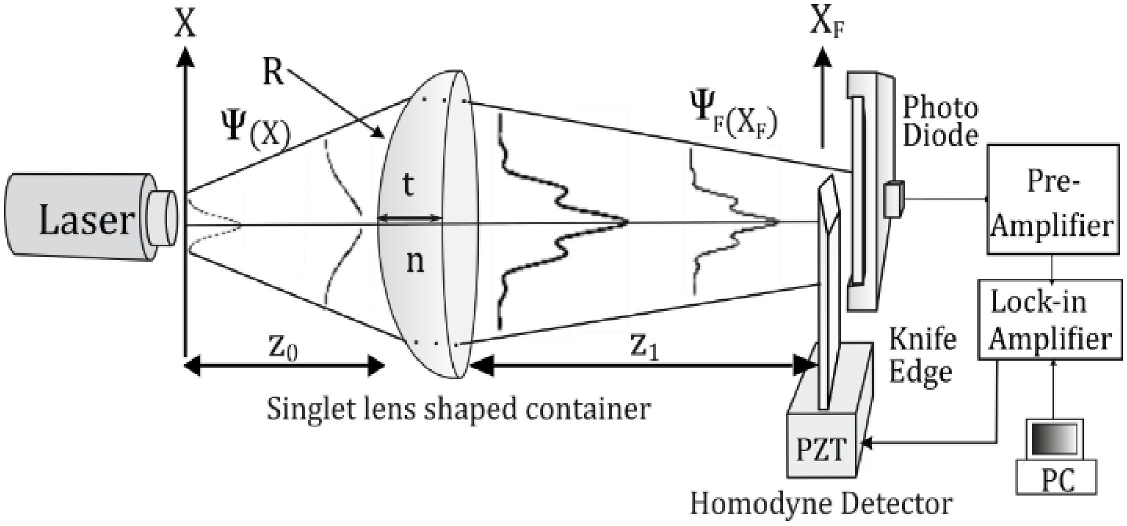

Fig. 3.7. High sensitivity mode optical setup using an SLSC. Optical setup of our proposal as described in the text. The SLSC is filled with the liquid sample.

We again use FGSI to calculate the normalized intensity profiles at different observation planes located at different distances z_1 placed close to the best focusing plane (BFP); in this case, BFP = 2.72 cm for a refractive index n_0 = 1.3317088, corresponding to pure tri-distilled water at room temperature [34, 35].

Change in the refractive indexes of the sample can be appreciated as the observation plane moves towards the sample or equivalently as z_1 decreases. We have recorded the normalized intensity profiles at twenty-one different observation planes, each one of them corresponding to an increase of the refraction index at equally spaced steps of 3.03×10^{-5}, thus, decreasing the focal length of the SLSC at each step. Fig.(3.8) depicts these plots. Plots with higher side-lobes heights correspond to observation planes with shorter z_1 values or equivalently, to higher n values. We have carefully chosen these twenty-one distances so that the heights of the analytical primary side-lobes coincide with those of our experimental glucose concentration measurements presented in the following section. The dot in Fig.(3.8) highlights the maximum vertical height of the left primary side-lobe for z_1= BFP – 185.9 μm.

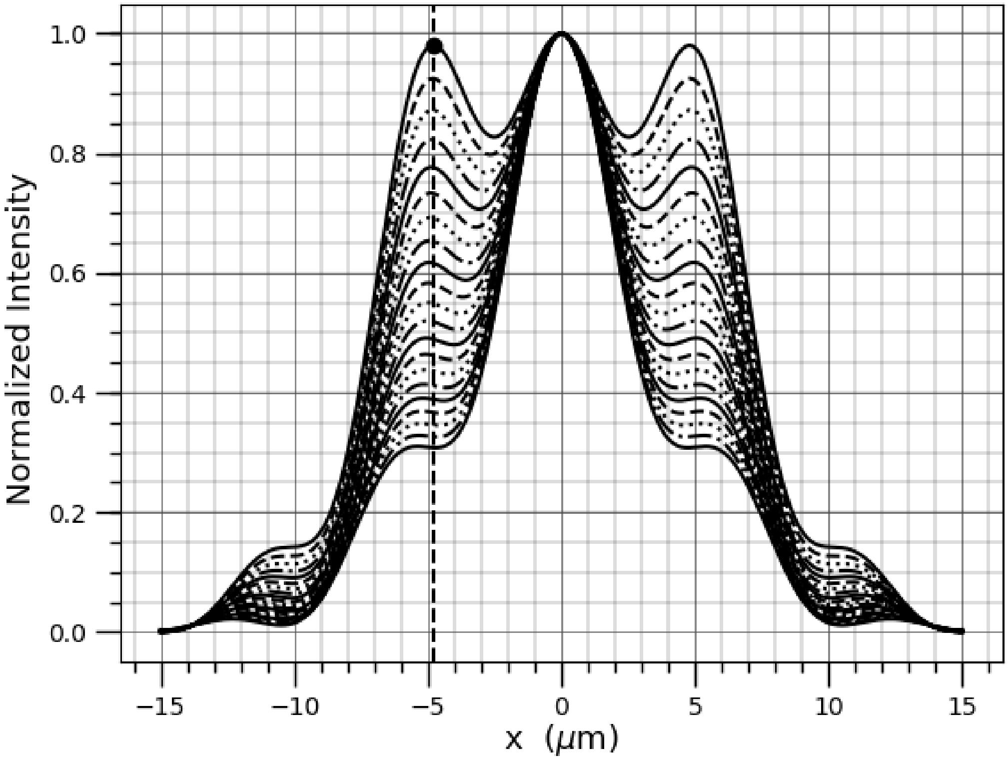

Fig. 3.8. Analytical normalized intensity profiles calculated by FGSI for the high sensitivity mode setup. Normalized intensity profiles calculated employing FGSI at different observation planes located at twenty-one different distances z_1 or obtained by changing the refractive index in steps of 3.03x10^{-5}. z_0= 5.0 m. The dot indicates the maximum left side-lobe height; z_1= BFP - 185.9 and n_0= 1.3317088.

Similarly, to the method described above for setting the height of the primary side-lobes that correspond to the sample of the lowest concentration C_0 = 0 mg/dl, we now set this height at 0.98 of the normalized intensity profile. We will refer to this initial setting as the initial plot and it will be characterized as $IPlot(C, h)$, where C, and h represent concentration in mg/dl and normalized height respectively. Therefore, our initial plot is represented as $IPlot(C_0, 0.98)$.

A summary of how the system is intended to be used may now be useful.

For measuring glucose concentration with our optical technique, first, the reference sample, with a concentration of 0 mg/dl is poured in the SLSC; this sample consists of pure tri-distilled water (n_0= 1.33171088). Then, the observation plane is placed at an appropriate distance z_1 that places the primary side-lobes at a height of approximately 0.98 of its normalized intensity profile. Taking into account that for our high mode system, samples with higher concentrations will cause a decrease in the heights of the side-lobes.

At this point, it may result interesting to note the behavior of a Gaussian free aberrated system. For this, we have performed experiments under the same conditions but reducing the distance between the laser and the SLSC to z_0= 80.0 cm. Fig. (3.9) depicts the resulting profiles. As the Gaussian beam is now free of aberrations, the sensitivity has been practically lost as the width of the Gaussian intensity profiles is maintained almost equal for each measurement.

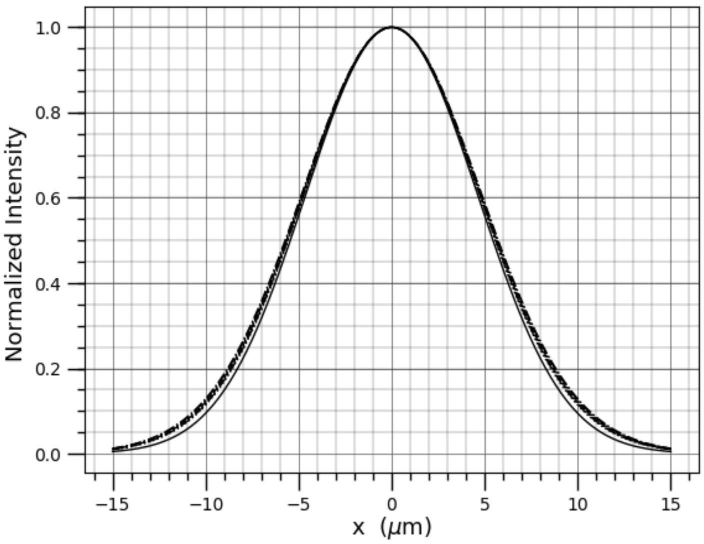

Fig. 3.9. Analytical normalized intensity profiles calculated by FGSI for a beam free of aberrations for high sensitivity measurements. Normalized intensity distributions at planes of observation placed at different z_1 distances within the overall range of the above case. z_0= 80.0 cm.

In the following section, we present the experimental results.

3.4 Experimental glucose measurements performed with a singlet-lens-shaped container (SLSC).

Applying the aforementioned method to perform the measurements, the experimental normalized intensity profiles corresponding to samples with concentrations ranging from 0 to 400 mg/dl in steps of 20 mg/dl are plotted in Fig.(3.10). The initial plot was set at $IPlot(C_0 = 0,0.98)$.

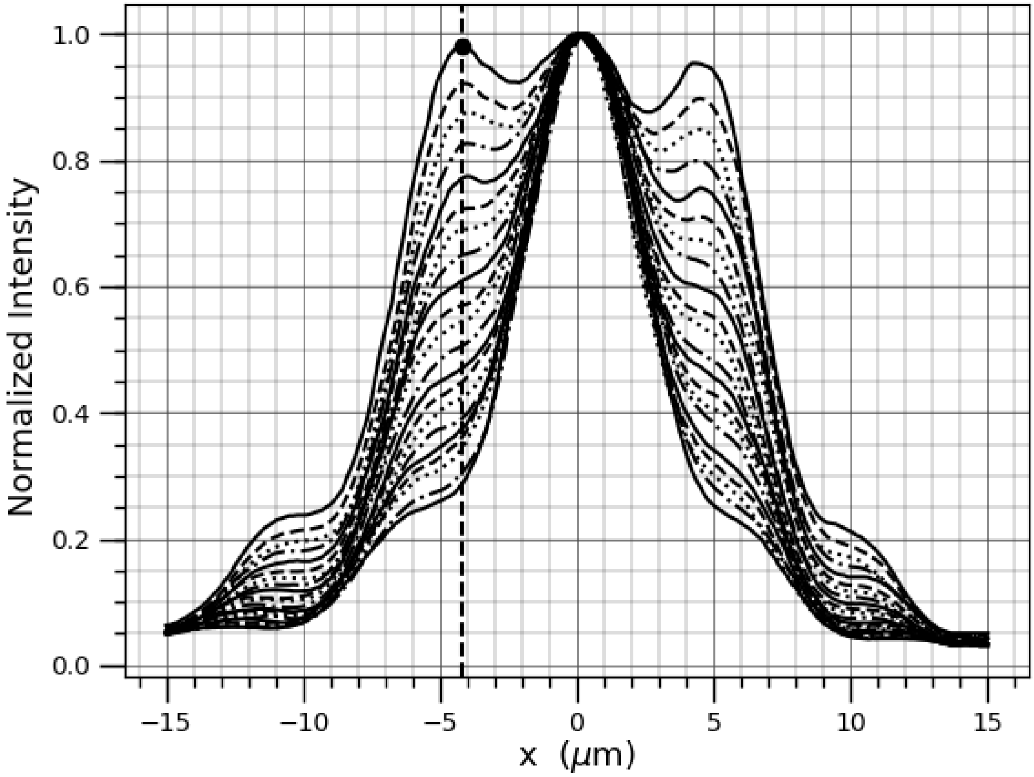

Fig. 3.10. Experimental normalized intensity distributions for the high mode setup. Experimental normalized intensity profiles for glucose concentrations ranging from 0 to 400 mg/dl in steps of 20 mg/dl. The plot with the highest left side-lobe vertical height corresponds to the initial plot (highlighted by a dot) for a sample of 0 mg/dl.

By comparing the theoretical Fig.(3.8) and the experimental Fig.(3.10), two main differences can be appreciated between them. Although these differences become irrelevant for glucose concentration measurement some comments are in order. The vertical heights of the left and right primary side-lobes are unequal and their roundness at low vertical heights is less accentuated. This is caused by undesired additional front superficial defects that are present in the SLSC. This is a result due to a lack of higher precision equipment for its construction and can be easily overcome with more efficient optical glass working tools.

Our analytical method is robust enough to allow us to simulate the above drawback. For this, we introduce in the FGSI equations an appropriate polynomial to represents the real front surface of the SLSC. Obviously, we do not have the experimental shape of the front surface, then, by a trial-and-error method, we found that in our case the required polynomial had a linear and fourth-order terms. Fig.(3.11) reveals the accuracy of the method by comparing these corresponding analytical normalized intensity profiles.

At this point, it should be stated that the calculations performed using FGSI to fit a suitable aberration polynomial to the front surface of the SLSC, were included exclusively to support properly our proposed technique, allowing us to compare the experimental and the analytical normalized intensity profiles. In an actual measurement, these calculations are not necessary as it is only required to calibrate the optical system within a region of interest by the procedure described above using appropriate reference samples.

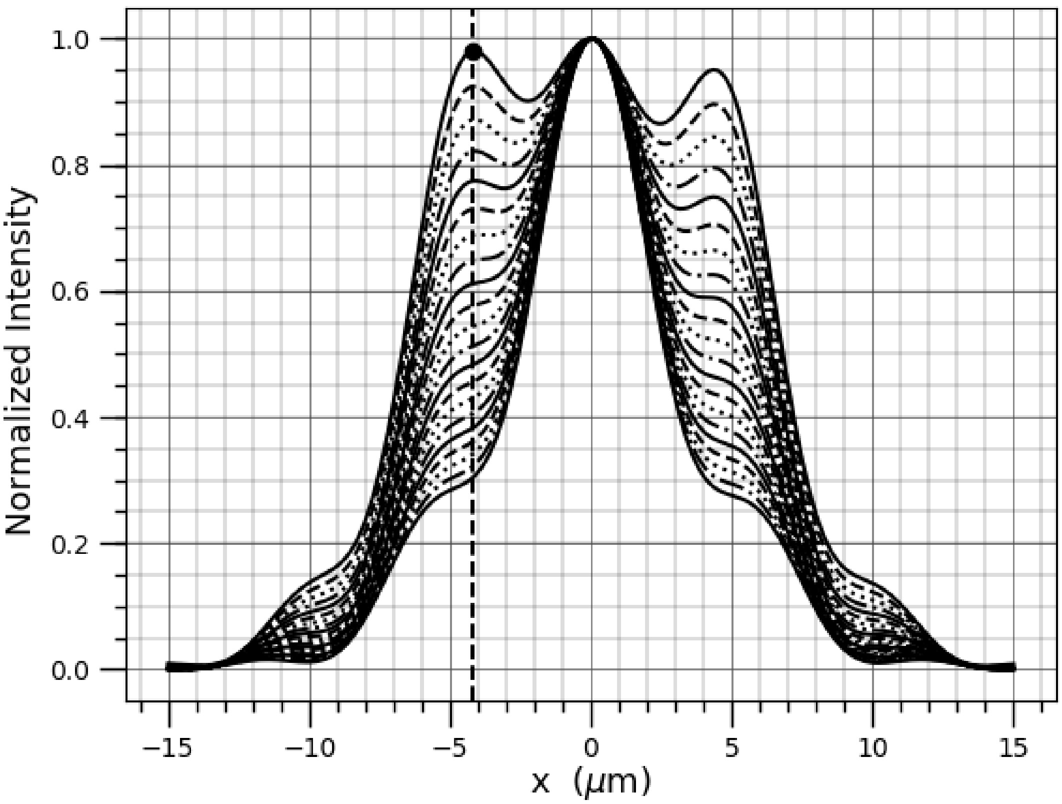

Fig. 3.11. Analytical normalized intensity distribution calculated by FGSI with a polynomial term. Analytical normalized intensity profiles obtained by FGSI introducing linear and fourth-order terms in the equation that represents the front surface of the SLSC.

To determine the analytical dependence between glucose concentration and the height of the primary side-lobes of the normalized intensity profiles, the experimental and analytical plots are aligned by placing their central peaks at the origin, as illustrated in Fig.(3.8), Fig(3.10), and Fig(3.11). Secondly, a vertical line that intersects the maximum height of the highest left side-lobe, the one that corresponds to $IPlot(0, 0.98)$, is traced. Finally, each height is determined at the point of intersection of the vertical line with its corresponding plot. In this way, a table relating the vertical heights, the sample refractive indexes, and the corresponding sample concentrations can be constructed. For brevity, Table 1 shows only eight of the twenty-one rows obtained from the plots of Fig.(3.8), Fig(3.10), and Fig(3.11).

		Left primary side-lobe heights		
Glucose concentration (mg/dl)	Refractive index	Fig. (3.8)	Fig. (3.10)	Fig. (3.11)
0	1.3317088	0.98	0.98	0.98
60	1.3317997	0.82	0.82	0.82
120	1.3318906	0.69	0.69	0.69
180	1.3319815	0.58	0.57	0.58
240	1.3320724	0.49	0.47	0.48
300	1.3321633	0.41	0.40	0.40
360	1.3322542	0.35	0.34	0.34
400	1.3323148	0.31	0.30	0.30

Table 3.1. Left side-lobe vertical heights obtained from the plots of Fig.(3.8), Fig(3.10), and Fig(3.11) for eight rows obtained by using the dashed vertical line with the method described in the text.

The data obtained for analytical and experimental plots are shown in Table (3. 1), these data confirm that the methodology described above is appropriate to determine the heights of the primary side-lobes accurately. Performing the above measurements several times we estimate an error of less than 2.0%.

Fig.(3.12) shows plots of the experimental left side-lobes heights measured with the methodology described above as a function of glucose concentration. The solid line shows the corresponding fitted curve.

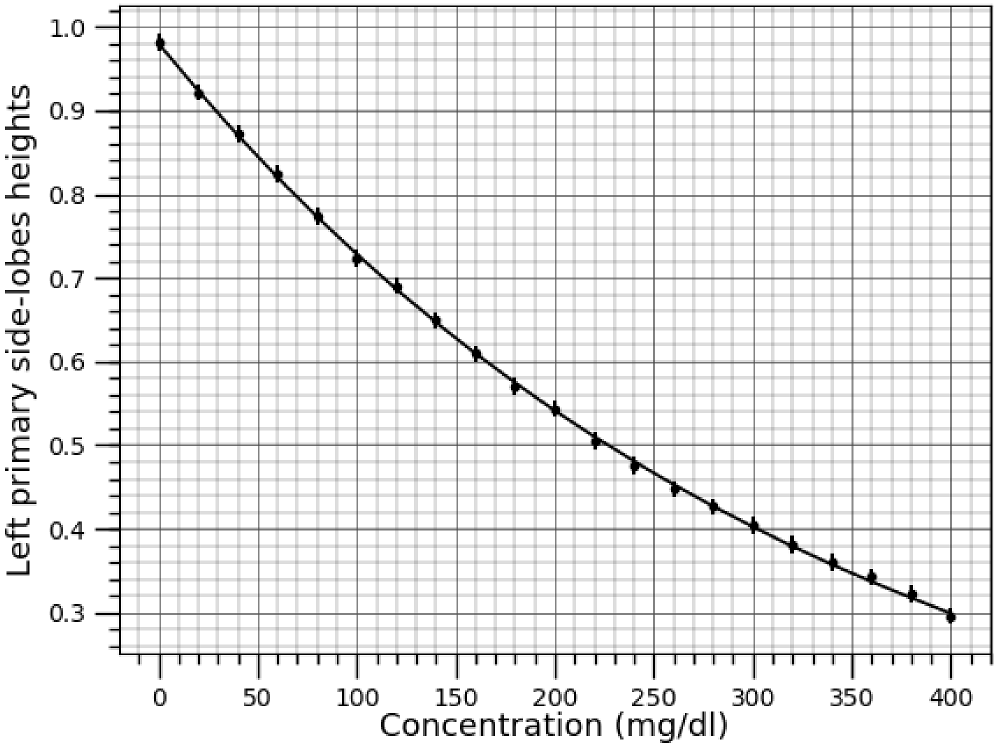

Fig. 3.12. Experimental heights as a function of glucose concentration for the second setup. Experimental heights of the primary left side-lobes as a function of glucose concentration.

The equation of the fitted curve is written as,

$$h(C) = 0.98\, exp(-2.966 \times 10^{-3} C)\,. \tag{3.3}$$

In Equation (3.3) h represents left side-lobe normalized height and C represents glucose concentration measured in mg/dl.

Using Equation (3.3) and assuming an uncertainty of the vertical heights of ±0.01 allows us to estimate the uncertainty of the technique as ± 6.23 mg/dl. This value is calculated at the central value of glucose concentration (200 mg/dl).

For our optical setup, setting the initial plot $IPlot(C_0, 0.98)$, allows us to generalize Equation (3.3) as,

$$h(C) = 0.98\, exp(-2.966 \times 10^{-3}) \times (C - C_0)\,, \tag{3.4}$$

where C_0 corresponds to the lowest concentration in the range under measurement. In this form accurate measurements, each 20 mg/dl can be performed in any range of interest. This is possible by using different initial plots (different initial concentrations C_0). For example, the precision of glucose concentrations measurements corresponding to low vertical heights of the previous experimental results, in the range from 300 to 400 mg/dl has an uncertain maximum height, so when establishing the initial plot to $IPlot(300, 0.98)$ the maximum height value is clearer and the data may have fewer errors. Proceeding in this way, similar plots to Fig.(3.10) are obtained, but this time the plot with the highest left side-lobe height corresponds to a concentration of 300 mg/dl. Making that the sensitivity of the technique can be extended to other fields in addition to clinical tests in which these high glucose ranges are out of interest. It is worth mentioning that, by performing several measurements in different ranges we have verified the repeatability of the proposed technique.

Although our preliminary experiments were conducted on samples containing only glucose [36], free of other substances that may be present in real clinical samples. It may result convenient to compare our predicted data measurements along with the results from a reference method, with the paired data points plotted on a Clarke error grid (CEG), currently used in clinical monitoring analysis [37, 38].

Following [15], the predicted measurements are plotted in a grid divided into five different regions denoted as A, B, C, D, and E. In region A the predicted measured concentrations do not differ by more than 20% of the reference. In the regions A and B, differences between the predicted values and the reference values do not represent a clinical risk for patients. On the other hand, errors in regions C, D, and E are significant and may lead to dangerous clinical decisions. As can be seen in Fig.(3.13) all the predicted concentrations obtained with our proposed technique for transparent pure tri-distilled water glucose solutions fall in satisfactory region A.

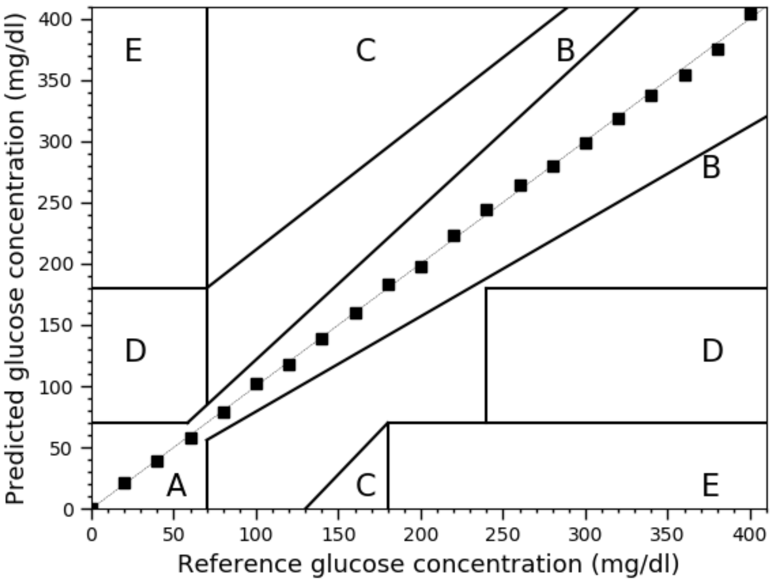

Fig. 3.13. Clarke Error Grid. Predicted glucose concentrations as a function of the reference concentrations.

In these glucose measurements, it was required only a small volume of the sample, about 0.3 ml to fill the SLSC container. This volume can be further decreased by reducing the front radius of the SLSC and diminishing its central inner thickness. This gives the added advantage of extending the applicability of our proposal for analyzing small-volume samples which is desirable for measuring many biofluids, as is the case of the glucose concentration measurement in aqueous humor or artificial aqueous humor [39] to determine the blood glucose concentration as described in [39-41].

Glucose measurement is an important application of this optical technique to measure concentrations in liquid samples making it possible to find the index of refraction with high sensitivity.

For example, for this particular application, it is possible to relate glucose concentration with refractive index using the theoretical plots and considering a linear relation as in [34, 35],

$$n(C) = 1.3317088 + mC \tag{3.5}$$

In Equation (15) n represents the refractive index and m is a constant.

Relating the experimental results with the theoretical plots we obtain m = (1.515± 0.094) $\text{x}10^{-6}$ which is in good agreement with [42].

Finally, the proposed technique provides improved stability compared with other methods since the illuminating beam only changes the semi-width by going through a different medium with a different index of refraction. Furthermore, temperature effects can be neglected since the probe beam is not focused inside the sample avoiding local heating that may cause vapor or micro-bubbles that alter the measurements.

4. Conclusions

We have demonstrated that if a Gaussian probe beam is allowed to attain high spherical aberrations it becomes highly sensitive on changes of the index of refraction of a liquid sample after being transmitted by it. By taking advantage of this new concept, we have introduced a new optical technique to measure with high accuracy and high repeatability changes of the index of refraction of liquid samples.

The technique presented here is based on measuring the heights of the primary side-lobes of the aberrated normalized intensity profile of the Gaussian probe beam after being transmitted by the liquid sample focused at a plane of observation. To improve even more the resolution of the measurements, the intensity profiles are accurately recorded employing a homodyne detector specially designed for this purpose.

We have demonstrated that the heights of the primary lateral side lobes of the normalized intensity profile change linearly on changes of the sample concentration.

To provide our optical technique with appropriate analytical support, we presented an analytical optical model based on the Fresnel Gaussian shape invariant method whose detailed description can be found in the literature. Based on our analytical results we have demonstrated that the optical technique may be employed in two different modes. In a first mode, referred to as the high sensitivity mode, the sample under test is poured in a singlet focusing lens-shaped container. In this mode, sensitivities in steps as low as 6 mg/dl can be obtained. In the low sensitivity mode, the sample under test is poured in a cuvette while a commercially available focusing singlet is used to focus the aberrated beam at a plane of observation. In the low sensitive mode, the measurements can be recorded in steps of 100mg/dl or larger.

As the high sensitivity mode falls appropriately in the range of clinical tests, we have tabulated our experimental results in a Clarke error grid to demonstrate that the optical technique fits well in the corresponding satisfactory safe region also referred to as region A.

Finally, it may be interesting to highlight that, as in the high sensitivity mode the beam is not focused inside the sample, perturbations due to local heating are highly reduced, improving the repeatability of the measurements.

Bibliography

[1] Wu, H., & Khan, M. (2012). THz spectroscopy: An emerging technology for pharmaceutical development and pharmaceutical Process Analytical Technology (PAT) applications. Journal of Molecular Structure, 1020, 112-120.

[2] Dinar, E., Riziq, A. A., Spindler, C., Erlick, C., Kiss, G., & Rudich, Y. (2008). The complex refractive index of atmospheric and model humic-like substances (HULIS) retrieved by a cavity ring down aerosol spectrometer (CRD-AS). Faraday discussions, 137, 279-295.

[3] Bandyopadhyay, S., Peralta-Videa, J. R., & Gardea-Torresdey, J. L. (2013). Advanced analytical techniques for the measurement of nanomaterials in food and agricultural samples: a review. Environmental Engineering Science, 30(3), 118-125.

[4] Yáñez, E., Cywiak, M., & Franco, S. J. M. (2019). Glucose Concentration Measurement of a Transparent Sample by Using a Gaussian Probe Beam with High Spherical Aberration. In Progress in Optomechatronic Technologies (pp. 111-115). Springer, Singapore.

[5] Ren, Z., Liu, G., Xiong, Z., & Huang, Z. (2015, July). Experiments of glucose solution measurement based on the tunable pulsed laser induced photoacoustic spectroscopy method. In Pacific Rim Laser Damage 2015: Optical Materials for High-Power Lasers (Vol. 9532, p. 95321Q). International Society for Optics and Photonics.

[6] Kottmann, J., Rey, J. M., & Sigrist, M. W. (2011). New photoacoustic cell design for studying aqueous solutions and gels. Review of Scientific Instruments, 82(8), 084903

[7] Yadav, J., Rani, A., Singh, V., & Murari, B. M. (2015). Prospects and limitations of non-invasive blood glucose monitoring using near-infrared spectroscopy. Biomedical signal processing and control, 18, 214-227.

[8] Liakat, S., Bors, K. A., Huang, T. Y., Michel, A. P., Zanghi, E., &Gmachl, C. F. (2013). In vitro measurements of physiological glucose concentrations in biological fluids using mid-infrared light. Biomedical optics express, 4(7), 1083-1090.

[9] Vilaboy, M. J., Ergin, A., Tchouassi, A., Greene, R., & Thomas, G. A. (2003, March). Optical measurement of glucose concentrations using Raman spectroscopy. In Bioengineering Conference, (2003) IEEE 29th Annual, Proceedings of (pp. 329-330). IEEE.

[10] A. K. Amerov, Y. Sun, G. W. Small, and M. A. Arnold, "Kromoscopic measurement of glucose in the first overtone region of the near-infrared spectrum," Proc. SPIE 4624, 11–20 (2002).

[11] Ansari, R. R., Boeckle, S., & Rovati, L. L. (2004). New optical scheme for a polarimetric-based glucose sensor. Journal of Biomedical Optics, 9(1), 103-116.

[12] K. V. Larin, M. Motamedi, T. V. Ashitkov, and R. O. Esenaliev, "Specificity of noninvasive blood glucose sensing using optical coherence tomography technique: a pilot study," Phys. Med. Biol. 48, 1371–1390 (2003).

[13] Moschou, E. A., Sharma, B. V., Deo, S. K., & Daunert, S. (2004). Fluorescence glucose detection: advances toward the ideal in vivo biosensor. Journal of fluorescence, 14(5), 535-547.

[14] A. Ghazaryan, S. V. Ovsepian, and V. Ntziachristos, "Extended near-infrared optoacoustic spectrometry for sensing physiological concentrations of glucose," Front. Endocrinol. 9, 112 (2018).

[15] M. K. Dasa, C. Markos, J. Janting, and O. Bang, “Multispectral photoacoustic sensing for accurate glucose monitoring using a supercontinuum laser,” J. Opt. Soc. Am. B 36, A61–A65 (2019).

[16] Al-Mbaideen, A. A., Rahman, T., & Benaissa, M. (2010, October). Determination of glucose concentration from near-infrared spectra using principle component regression coupled with digital bandpass filter. In Signal Processing Systems (SIPS), 2010 IEEE Workshop on (pp. 243-248). IEEE.

[17] J. Chen and X. Z. Wang, “A new approach to near-infrared spectral data analysis using independent component analysis,” J. Chem. Inf. Comput. Sci., vol. 41, (2001), pp. 992–1001.

[18] M. Cywiak, M. Servín, A. Morales, Diffractive and geometric optical systems characterization with the Fresnel Gaussian shape invariant, Opt. Express 19 (3) (2011) 1892–1904.

[19] M. Cywiak, A. Morales, J. M. Flores, M. Servín, Fresnel-Gaussian shape invariant for optical ray tracing, Opt. Express 17(13) (2009) 10564–10572.

[20] M. Cywiak, M. Servín, and F. Mendoza-Santoyo, “Wave-front propagation by Gaussian superposition,” Opt. Commun. 195(5-6), 351–359 (2001).

[21] M. Cywiak, M. Servín, and A. Morales, “Diffractive and geometric optical systems characterization with the Fresnel Gaussian shape invariant,” Opt. Express 19 (3), 1892-1904 (2011).

[22] Goodman, J. W. (2005). Introduction to Fourier optics. Roberts and Company Publishers.

[23] Stamnes, Jakob J. Waves in Focal Regions: propagation, diffraction and focusing of light, sound and water waves. CRC Press, (1986), 336-337.

[24] Cywiak, M., Cywiak, D., & Yáñez, E. (2017). Finite Gaussian wavelet superposition and Fresnel diffraction integral for calculating the propagation of

truncated, non-diffracting and accelerating beams. Optics Communications, 405, 132-142.

[25] Milonni, P., & Eberly, J. (1988). Laser resonators. Lasers, John Wiley & Sons, New York, 486.

[26] Arfken, G. B., & Weber, H. J. (1999). Mathematical methods for physicists.

[27] Siegman, A. E. Lasers University Science Books, Mill Valley, CA, 1986. This book contains an in-depth description of the usefulness of viewing Gaussian beams as a complex source point on, 637-641

[28]Thyagarajan, K., & Ghatak, A. (2010). Lasers: fundamentals and applications. Springer Science & Business Media.

[29] Renard, E. (2005). Monitoring glycemic control: the importance of self-monitoring of blood glucose. The American journal of medicine, 118(9), 12-19.

[30] Tuchin, V. V. (Ed.). (2008). Handbook of optical sensing of glucose in biological fluids and tissues. CRC press.

[31] McNichols, R. J., & Cote, G. L. (2000). Optical glucose sensing in biological fluids: an overview. Journal of biomedical optics, 5(1), 5-17.

[32] Khalil, O. S. (1999). Spectroscopic and clinical aspects of noninvasive glucose measurements. Clinical chemistry, 45(2), 165-177.

[33] Cervantes-L, J., Cywiak, M., Olvera-R, O., & Cywiak, D. (2014). Measurement of glucose concentration in a thin turbid medium by a transmitted Gaussian beam. Optics Communications, 331, 239-243.

[34] Tuchin, V. V., Maksimova, I. L., Zimnyakov, D. A., Kon, I. L., Mavlyutov, A. H., & Mishin, A. A. (1997). Light propagation in tissues with controlled optical properties. Journal of biomedical optics, 2(4), 401-418.

[35] Tuchin, V. V., Maksimova, I. L., Kochubey, V. I., Kon, I. L., Mavlyutov, A. H., Mishin, A. A., ... & Zimnyakov, D. A. (1997, August). Optical and osmotic properties of human sclera. In Optical Tomography and Spectroscopy of Tissue: Theory, Instrumentation, Model, and Human Studies II (Vol. 2979, pp. 658-676). International Society for Optics and Photonics.

[36] Yáñez, E., Cywiak, M., & Cywiak, D. (2019). Gaussian beam with high spherical aberration focused by a singlet lens-shaped container for glucose measurements. Applied Optics, 58(31), 8495-8500.

[37] Klonoff, D. C. (2012). The need for clinical accuracy guidelines for blood glucose monitors.

[38] Pfützner, A., Mitri, M., Musholt, P. B., Sachsenheimer, D., Borchert, M., Yap, A., & Forst, T. (2012). Clinical assessment of the accuracy of blood glucose measurement devices. Current medical research and opinion, 28(4), 525-531.

[39] Lambert, J. L., Pelletier, C. C., & Borchert, M. S. (2005). Glucose determination in human aqueous humor with Raman spectroscopy. Journal of Biomedical Optics, 10(3),

[40] Pohjola, S. (1966). The glucose content of the aqueous humour in man. Acta ophthalmologica, Suppl-88.

[41] Schrader, W. F., Grajewski, R. S., & Meuer, P. (2000, March). The glucose content of the aqueous humour compared with capillary blood man. In INVESTIGATIVE OPHTHALMOLOGY & VISUAL SCIENCE (Vol. 41, No. 4, pp. S77-S77). 9650 ROCKVILLE PIKE, BETHESDA, MD 20814-3998 USA: ASSOC RESEARCH VISION OPHTHALMOLOGY INC.

[42] Maier, J. S., Walker, S. A., Fantini, S., Franceschini, M. A., & Gratton, E. (1994). Possible correlation between blood glucose concentration and the reduced scattering coefficient of tissues in the near infrared. Optics letters, 19(24), 2062-2064.